designs

MDPI

Article

Design and Evaluation of Chaos-Based Excitation Strategies for Brushless DC Motor Drives: A Multi-Domain Framework for Application-Specific Selection

Asad Shafique [1], Georgii Kolev [1], Oleg Bayazitov [2], Varvara Sheptunova [2] and Ekaterina Kopets [1,*]

[1] Youth Research Institute, Saint Petersburg Electrotechnical University "LETI", 5 Professora Popova St., 197022 Saint Petersburg, Russia; ashafik@stud.etu.ru (A.S.); gyukolev@etu.ru (G.K.)
[2] Computer-Aided Design Department, Saint Petersburg Electrotechnical University "LETI", 5 Professora Popova St., 197022 Saint Petersburg, Russia; oobaiazitov@etu.ru (O.B.); vesheptunova@etu.ru (V.S.)
* Correspondence: eekopets@etu.ru

Abstract

This paper presents the design and multi-domain evaluation of three chaos-based excitation strategies for brushless DC (BLDC) motor drives implemented using Chua circuit-generated deterministic chaotic signals injected at three distinct control points: the PWM duty cycle, the commutation sequence, and the current feedback loop. A systematic design methodology is established for each injection architecture, including signal normalization, amplitude parameterization, and injection point characterization, evaluated across the electromagnetic, thermal, mechanical, and acoustic domains through MATLAB (R2024a) simulation and physical test stand validation. PWM injection produces controlled spectral dispersion with 5–7% speed reduction and a 10–15 dB SNR decrease, making it the recommended design choice for acoustic signature masking in stealth UAV applications. Commutation injection achieves severe system destabilization with speed reduction exceeding 56% and SNR losses greater than 30 dB, establishing it as a design tool for accelerated stress testing and fault emulation. Current feedback injection delivers a balanced excitation profile with 12–20% efficiency loss and 16–30% SNR reduction, making it suitable as a design method for online parameter identification and adaptive control development. This study establishes the first multi-domain comparative design framework for application-specific selection of chaos excitation strategies in BLDC drives, supported by nonparametric statistical validation and experimental acoustic confirmation, providing drive engineers with quantitative selection criteria across four physical domains.

Keywords: engineering design methodology; brushless DC motor drive; Chua circuit; chaos-based excitation; PWM design; multi-domain performance evaluation; application-specific selection; acoustic signature control; stealth UAV design; system robustness

Check for updates

Academic Editor: Mateusz Dybkowski

Received: 24 January 2026
Revised: 5 March 2026
Accepted: 9 March 2026
Published: 17 March 2026

Copyright: © 2026 by the authors. Licensee MDPI, Basel, Switzerland. This article is an open access article distributed under the terms and conditions of the Creative Commons Attribution (CC BY) license.

1. Introduction

High energy conversion efficiency, high power density and controllability have made brushless DC (BLDC) motors an indispensable element of modern electric propulsion and automation systems [1,2]. These motors are widely used in electric vehicles, industrial robotics, renewable energy conversion systems, and unmanned aerial vehicles (UAVs), where their benefits in operational reliability and performance have led to rapid uptake in a variety of industries. The further development of BLDC technology, especially in the attainment of low-cost, high-performance designs, has made possible the expansion of

commercial drones and other uses that need agile dynamics, long-range operations, and multi-axis control functionality.

Although conventional BLDC motor control methods are widely used, they have serious limitations. Conventional methods like Proportional–Integral–Derivative (PID) control, Field-Oriented Control (FOC) and Direct Torque Control (DTC) provide a good performance in linear operating conditions with constant conditions [2–4]. Nevertheless, these approaches find it difficult to deal with nonlinear motor dynamics, time-dependent parameter variations, external perturbations, and acoustic signature control. Acoustic noise control is especially problematic in stealth-sensitive applications like military surveillance UAVs, covert operations, and wildlife monitoring, where the tonal frequencies of BLDC motors can be a problem for detectability. The current control measures do not have effective mechanisms of maintaining performance and obscuring acoustic signatures at the same time, which is a major weakness that limits its application in sensitive operational environments.

This paper addresses these challenges by thoroughly examining chaos-based control of BLDC motor drives. This study uses chaos theory and deterministic characteristics of chaotic systems to improve the robustness of motor drives, allow for faster fault simulation, and minimize acoustic detectability by dispersion of spectral energy [5,6]. Compared to stochastic processes, chaotic systems are sensitive to the initial conditions and have aperiodic trajectories and complex attractors. In contrast to random noise injection, chaotic signals offer structure complexity that can be specifically designed to enhance system identification, fault detection, and resilience to perturbations as seen in power electronics and industrial drive applications [7]. The circuit used in this work to produce deterministic chaotic signals, which are injected at three different control points, is the circuit of Chua [8–10]. The overall test measures the effects on the signal-to-noise ratio (SNR), speed stability, thermal behavior, mechanical vibration, and acoustic emissions. One of the novelties is the creation of a single software–hardware platform, which allows one to compare injection strategies in various physical domains systematically prior to hardware implementation.

This research addresses three critical gaps in the existing literature. Although chaotic behavior has been reported in BLDC motors due to PWM nonlinearities [11], its intentional use as a control mechanism remains underexplored. Furthermore, the existing chaos-based motor control studies focus predominantly on single injection points without cross-strategy comparison, and multi-domain evaluation combining electrical, thermal, mechanical, and acoustic analyses is absent from this work. This study tests the hypothesis that strategic injection of Chua circuit-generated signals at different control points produces distinct, application-specific performance trade-offs. Specifically, three questions are addressed: (1) Can PWM injection disperse spectral energy to obscure acoustic signatures without serious performance degradation? (2) Can commutation injection serve as an accelerated stress testing method during controlled instabilities? (3) Can current feedback injection provide balanced system excitation for online parameter identification and adaptive control? These questions are addressed through multi-domain simulation validated by physical experimentation, offering a comprehensive framework for application-specific selection of chaos-based control strategies in BLDC motor systems.

The remainder of this paper is organized as follows. Section 2 reviews the chaos theory fundamentals, the Chua circuit, BLDC motor modeling, and positions chaos-based control relative to modern control approaches. Section 3 presents the system modeling methodology, including motor, thermal, and acoustic models, the three injection strategies, and the experimental design. Section 4 reports the simulation and experimental results for each injection strategy with statistical analysis. Section 5 discusses the results, compares the

findings against the existing literature, and outlines practical implementation guidelines and future research directions. Section 6 presents the conclusions.

2. Literature Review and Theoretical Background

2.1. Chaos Theory in Engineering Systems

Chaos theory is based on systems whose dynamic properties produce significantly disparate results due to small changes in the initial conditions [5]. Features of chaos make it worthwhile for various engineering tasks, as unpredictable behavior can increase system reliability, facilitate sophisticated fault detection, and enhance the discovery of essential parameters. This phenomenon is described in Lorenz's study of atmospheric air currents, which laid the foundation for future research in this field. In this work, Lorenz demonstrated that minor disturbances within a system can give rise to substantial variations in time. A study by Poincaré of the three-body problem was the first work in the field to provide fundamental ideas that remain the building blocks of chaos theory. A dynamical system is generally presumed to be chaotic, with its mathematical modeling encompassing nonlinear terms within differential equations. The time-dependent behavior of a typical dynamical system can be regarded as a representation of this system:

$$\frac{dx}{dt} = f(x, t, p) \tag{1}$$

With specific nonlinear effects that cause chaotic behavior, the system's dynamics switch to aperiodic behavior and depend significantly on the initial conditions, which can be proven by the Lyapunov exponent λ:

$$\lambda = \lim_{n\to\infty} \frac{1}{t} \ln \left| \frac{\|\delta x(t)\|}{\|\delta x(0)\|} \right| \tag{2}$$

2.2. Chua's Circuit: Mathematical Foundation and Engineering Relevance

The Chua circuit, first demonstrated by Chua, Komuro, and Matsumoto in their seminal 1984 work on the double-scroll family [8], is one of the fundamental electrical circuits capable of exhibiting deterministic chaotic behavior. The circuit consists of two capacitors (C_1 and C_2), one inductor (L), one resistor (R), and one nonlinear resistor (Chua diode). This autonomous three-dimensional system produces the famous double-scroll attractor that has become a paradigm for experimental and theoretical chaos research, with comprehensive analysis provided in later works by Chua [12] and systematic implementation guidelines given by Kennedy [9] and Madan [10]. The system dynamics are described by the following equations:

$$C_1 \frac{dv_{C1}}{dt} = \frac{1}{R}(v_{C2} - v_{C1}) - g(v_{C1}) \tag{3}$$

$$C_2 \frac{dv_{C2}}{dt} = \frac{1}{R}(v_{C1} - v_{C2}) + i_L \tag{4}$$

$$L \frac{di_L}{dt} = -v_{C2} \tag{5}$$

Here, $g(v_{C1})$ represents the nonlinear function of Chua's diode, mathematically defined as given:

$$g(v_{C1}) = m_1 v_{C1} + \frac{1}{2}(m_0 - m_1)(|v_{C1} + E| - |v_{C1} - E|) \tag{6}$$

In circuit analysis, a curve is divided into segments before and after the breakpoint voltage E. These segments are labeled, respectively, inner (m_0) and outer (m_1) slopes. In order to be the object of rigorous investigation and simulation, such apparent areas will be expressed in terms of scale and time, with the relevant variables being suitably modified to ensure comprehensive coverage of the phenomenon.

$$\frac{dx}{dt} = \alpha(y - x - f(x)) \tag{7}$$

$$\frac{dy}{dt} = x - y - z \tag{8}$$

$$\frac{dz}{dt} = -\beta y \tag{9}$$

Standard parameters ($\alpha = 20$, $\beta = 40$, $m_0 = -1.143$, $m_1 = -0.714$) typically produce a double-scroll attractor. This nonlinear function and the subsequent normalized state-space representation have been widely studied since Chua's original work [8] and comprehensively analyzed by Kennedy [9] and Madan [10] for circuit implementation and parameter selection, with the 1993 monograph [13] providing a comprehensive explanation of the paradigm.

Although the classical Chua circuit uses a physical inductor, more recent developments have proposed simplified versions that maintain the important dynamics of double scrolls, but allow for easy digital implementation [14,15]. Such inductor-less designs are especially applicable to embedded motor control systems where physical circuit size and numerical integration performance are important.

The discrete-time Chua map proposed by Altman and Itoh [14] eliminates the inductor by reformulating the dynamics as follows:

$$x_{n+1} = y_n \tag{10}$$

$$y_{n+1} = z_n \tag{11}$$

$$z_{n+1} = -\alpha z_n - \beta y_n + \gamma f(x_n) \tag{12}$$

where $f(x_n)$ is a piecewise-linear approximation of the Chua diode characteristic. This form allows for direct implementation via difference equations with fixed-point arithmetic on low-cost microcontrollers, achieving computational efficiency of <50 μs per iteration on ARM Cortex-M4 processors [14].

2.3. BLDC Motor Modeling and Control: Traditional Approaches and Limitations

The operation of BLDC motors is modeled using complex computer simulations. These motors are equipped with permanent magnet rotors and are subject to electronic control. The fundamental voltage equations for a three-phase system are expressed as follows:

$$u_a = R_s i_a + L_s \frac{di_a}{dt} + e_a \tag{13}$$

$$u_b = R_s i_b + L_s \frac{di_b}{dt} + e_b \tag{14}$$

$$u_c = R_s i_c + L_s \frac{di_c}{dt} + e_c \tag{15}$$

These three-phase voltage equations are the standard form for BLDC motor electrical dynamics, as established by Krishnan [2], Hanselman [1], and early drive system analyses [16].

Rs and Ls represent phase resistance and inductance, respectively, and e_a, e_b, e_c are back EMF terms proportional to rotor speed ω_m and electrical position θ_e:

$$ea = ke\omega mfa(\theta e) \tag{16}$$

$$eb = ke\omega mfb(\theta e) \tag{17}$$

$$ec = ke\omega mfc(\theta e) \tag{18}$$

Mechanical dynamics are based on the concept of torque projection.

$$J\frac{d\omega_m}{dt} = T_c - T_L - B\omega_m \tag{19}$$

Thermal changes are modeled by using lumped parameter models:

$$C_{th,\omega}\frac{dT_\omega}{dt} = P_{Cu} + P_{Fe} - \frac{T_\omega - T_h}{R_{th,\omega h}} \tag{20}$$

$$C_{th,h}\frac{dT_h}{dt} = \frac{T_\omega - T_h}{R_{th,\omega h}} - \frac{T_h - T_{amb}}{R_{th,ha}} \tag{21}$$

The lumped-parameter thermal network model is a common model for the thermal analysis of electric motors. It has two nodes (winding and housing), is well known in the thermal modelling literature and is widely used in motor design practice [1,2]. This model strikes a balance between computational performance and the accuracy required to predict the transient thermal response of small-to-medium power motors.

Conventional speed and torque controllers are predicated on linear theories and traditional control loops to ensure stability. However, these approaches also have some limitations, particularly in terms of their ability to effectively address changes in behavior and external influences.

2.4. Related Work in Chaotic Control of Motor Drives

Chaos theory has gained widespread application in motor control systems over the last few years, with numerous studies examining its various applications [17]. Li et al. [11] examined chaotic pulse-width modulation (PWM) methods for induction motor drives. However, they also noted an increase in total harmonic distortion (THD) by 10–15%, consistent with the THD performance trade-offs documented in conventional PWM inverter analysis [18]. The study concluded that the use of chaotic modulation results in the distribution of electrical energy over a wide range of frequencies and a reduction in the motor's peak emissions. In contrast to the conventional pseudo-random binary sequences, Zhang and Wang [19] opted for chaotic sequences to ascertain critical parameters for motor drives. Consequently, they achieved a convergence rate that was 25% faster than previously attained. This research facilitates the observation of the valuable effects of chaotic excitation, which can significantly aid in identifying BLDC motor systems. In a recent study, Petrov et al. [20] developed novel methodologies for noise control, resulting in a 10 dB reduction in noise levels in motor drives.

Random PWM techniques have been widely studied as a conventional approach to spectral spreading in motor drives [21–23], with Trzynadlowski et al. [24] providing a comprehensive review of strategies that redistribute harmonic energy through randomized switching frequency. However, these methods rely on stochastic randomness rather than a deterministic chaotic structure. The optimal PWM strategies [25,26] attempt to address this by solving harmonic elimination problems, but do so at the cost of fixed harmonic spectra that cannot be dynamically shaped for application-specific requirements. A significant

number of literature sources focus on a single chaotic excitation strategy, and obtaining a proper measurement of essential factors, such as the SNR, is quite rare.

2.5. Comparison with Modern Control Approaches

Although chaos-based control is a new paradigm in the use of BLDC motors, it is important to put this method into context with the larger picture of advanced control methods that are currently being used to control nonlinear systems and disturbance rejection.

2.5.1. State Feedback and Disturbance Rejection Control

Control theory of modern times provides a number of proven methods of dealing with nonlinearities and disturbances in motor drives. The state feedback control that has an integral action offers a strong tracking performance and disturbance rejection properties [3,4]. These techniques are based on proper estimation of states, which is usually achieved by observers or Kalman filters [27], to estimate the unmeasured states based on the sensor data. Nevertheless, state feedback controllers require accurate system models and cannot readily accommodate unmodeled dynamics and parametric uncertainties [3,4], which are pervasive in real-world motor drive systems due to temperature-dependent winding resistance, magnetic saturation at high current densities, and progressive mechanical wear [2].

2.5.2. Sliding Mode Control (SMC)

Sliding mode control has received a lot of interest in motor drive applications because of its natural resistance to changes in parameters and external disturbances [28]. SMC constrains the system path to a prescribed sliding surface in which one can achieve the desired dynamics despite limited uncertainties. The discontinuous switching of SMC offers great disturbance rejection, but introduces chattering effects that excite unmodeled high-frequency dynamics and amplify acoustic noise in motor windings and housing structures [29], which is directly counterproductive in the stealth applications targeted in this work. Higher-order sliding mode methods reduce chattering through boundary layer approximations, but at the cost of increased computational complexity and the need to tune additional boundary layer parameters [29].

2.5.3. Multilayer Neural Network and Adaptive Control

Multilayer neural networks have been effectively used in motor control issues, especially in learning inverse dynamics models and nonlinearities compensation [30]. Adaptive neural network controllers are able to modify their parameters online to suit the changing operating conditions and system uncertainties. Nevertheless, these methods have a number of well-documented limitations in motor drive applications [30–32]: (1) they require large amounts of labeled training data spanning the full operating envelope, which is expensive to collect for rotating machines under varying load and temperature conditions; (2) they lack formal guarantees of stability and convergence under rapidly varying disturbances, unlike Lyapunov-based classical controllers; (3) they impose significant computational demands that exceed the resources available on low-cost embedded motor controllers; and (4) the learned representations provide limited physical interpretability, making fault diagnosis and parameter tuning difficult.

2.5.4. Reinforcement Learning (RL) for Nonlinear Systems

RL controllers are trained to identify optimal control policies by interacting with systems or high-fidelity simulators and can discover strategies that surpass conventional controllers in specific operating regimes [33,34]. Recent extensions to electric motor drives have demonstrated promising results in current regulation, speed tracking, and energy optimization for PMSM and BLDC systems [35]. However, RL-based methods present several

limitations that are relevant to the objectives of this paper [35]. First, training requires from thousands to millions of interaction episodes, which is impractical for real motor hardware where prolonged operation at non-optimal operating points causes wear and thermal stress; second, learned policies are not physically interpretable, making it impossible to reason about their behavior in novel operating conditions or to extract physical parameters; third, enforcing safety constraints during online exploration is fundamentally difficult and can result in hardware damage through overcurrent or overspeed events; and fourth, the resulting controllers are black-box neural networks that cannot be readily adapted for domain-specific objectives such as acoustic signature shaping or fault emulation.

3. Methodology and System Modeling

This section outlines a consistent approach to examining chaotic control systems for BLDC electric motors, primarily through simulation, ensuring that steps can be followed with real hardware. The methodology utilizes detailed mathematical models of the BLDC motor, which encompass electrical, thermal, mechanical, and acoustic properties, and then injects chaotic signals using specialized computer programs.

3.1. BLDC Motor Model

The BLDC motor model has been constructed with the objective of supporting heterogeneous dynamics that are observed in different application scenarios. Consequently, this model enables the systematic analysis of chaotic injection phenomena.

The model delineates the electrical equilibrium of a three-phase system, the equations of which are as follows. These equations are based on the parameters of a BLDC system.

$$u_a = R_s i_a + L_s \frac{di_a}{dt} + e_a \tag{22}$$

$$u_b = R_s i_b + L_s \frac{di_b}{dt} + e_b \tag{23}$$

$$u_c = R_s i_c + L_s \frac{di_c}{dt} + e_c \tag{24}$$

The back-EMF terms are expressed as follows:

$$e_a = k_e \omega_m \sin(\theta_e), \tag{25}$$

$$e_b = k_e \omega_m \sin(\theta_e - 2\pi/3), \tag{26}$$

$$e_c = k_e \omega_m \sin(\theta_e - 4\pi/3), \tag{27}$$

It should be noted that Equations (25)–(27) employ sinusoidal back-EMF functions rather than the trapezoidal waveforms that characterize ideal BLDC motor operation [2]. A true BLDC motor produces trapezoidal back-EMF with flattop regions spanning 120 electrical degrees per half-cycle, arising from the concentrated winding distribution and surface-mounted permanent magnet geometry [1,2]. The sinusoidal approximation is, however, widely adopted in simulation studies of six-step commutated drives when the primary objective is the analysis of control-loop dynamics, spectral spreading behavior, and cross-domain performance comparisons rather than precise torque ripple characterization [2,17]. The sinusoidal model faithfully captures the fundamental electrical equilibrium described by Equations (22)–(24), the speed regulation dynamics, the thermal power dissipation through copper and iron losses, and the current harmonic structure that drives the acoustic pressure model in Equations (31) and (32). The principal effect of using a trapezoidal rather than sinusoidal back-EMF would be a modification of the commutation

torque ripple magnitude and the specific harmonic content of the phase current waveforms. These effects alter the absolute values of acoustic SPL and vibration metrics at the commutation frequency and its harmonics, but do not change the directional response to chaotic injection across any of the four evaluated domains. A study by Chen and Cao [17], which surveys chaos-based control in BLDC drives, confirms that sinusoidal approximations are standard practice in this class of simulation study. Full trapezoidal back-EMF modelling with hardware-in-the-loop validation is identified as a direction for future work

The mechanical behavior is modeled using the fundamental torque balance equation:

$$J\frac{d\omega_m}{dt} = T_e - T_L - B\omega_m \tag{28}$$

Understanding thermal dynamics is essential for evaluating the long-term sustainability of chaotic control strategies and identifying potential overheating issues. A two-node lumped parameter thermal network is used to balance computational efficiency with sufficient accuracy for predicting the temperature of the motor windings [1,2]. The thermal model consists of two coupled first-order differential equations representing the winding temperature T_w and housing temperature T_h.

$$C_{th,w}\frac{dT_w}{dt} = P_{Cu} + P_{Fe} - \frac{T_w - T_h}{R_{th,wh}} \tag{29}$$

$$C_{th,h}\frac{dT_h}{dt} = \frac{T_w - T_h}{R_{th,wh}} - \frac{T_h - T_{amb}}{R_{th,ha}} \tag{30}$$

The thermal model parameters are defined as follows:

The acoustic emissions of BLDC motors arise from three primary mechanisms: electromagnetic force ripples, mechanical vibrations transmitted through the motor housing, and aerodynamic effects [36,37]. For the purposes of this simulation study, acoustic pressure is estimated using a simplified linear superposition model combining electromagnetic and mechanical contributions [13]:

$$SPL = 20\log_{10}\left(\frac{P_{rms}}{P_{ref}}\right) \tag{31}$$

where P_{ref} = 20 μPa is the standard reference acoustic pressure in air. The RMS acoustic pressure P_{rms} is derived from electromagnetic force pulsations and mechanical vibrations, where $F_{em,rms}$ is determined from the magnetic field distribution in the motor [38], using an empirically validated relationship for small BLDC motors [39]:

$$P_{rms} = K_{em}\sqrt{F_{em,rms}^2} + K_{mech}\sqrt{a_{vib,rms}^2} \tag{32}$$

Here, K_{em} = 0.005 Pa/N is electromagnetic-force-to-pressure conversion factor, and $F_{em,rms}$ is the electromagnetic force ripple calculated from current harmonics and flux density, with K_{mech} being the mechanical-vibration-to-pressure conversion factor.

This formulation is intended to capture relative spectral changes induced by chaotic injection rather than calibrated absolute sound pressure levels. The actual relationship between electromagnetic force and acoustic pressure is nonlinear in practice, involving structural resonances, radiation impedance, and vibroacoustic coupling that are not represented by Equations (31) and (32) [37,40]. Full vibroacoustic characterization following requires a calibrated measurement environment and is beyond the scope of this simulation study.

Figure 1 contextualizes the scope of the model across three panels. The left panel presents the peak SPL values measured on the physical test stand (Section 4.5) for five control strategies, which are calibrated experimental measurements. The reduction from 82 dB under baseline PID to 71 dB under chaos PWM S5 represents an 11 dB peak SPL reduction and constitutes the primary acoustic claim of this paper. The center panel illustrates the spectral broadening mechanism predicted by the acoustic model; energy concentrated at discrete commutation harmonics under baseline operation is redistributed across a wider bandwidth under chaotic injection, which is consistent with the spectrograms. The right panel explicitly delineates the boundary between what the simulation model quantifies and what requires physical measurement. Absolute SPL values under high-perturbation conditions, in particular the commutation injection values reported, are indicative model-domain outputs produced by the unsaturated linear conversion in Equation (32) and should not be compared against physical references. The relative spectral changes and directional SPL trends across injection strategies remain physically meaningful and are supported by the experimental measurements in Section 4.5 [13,40].

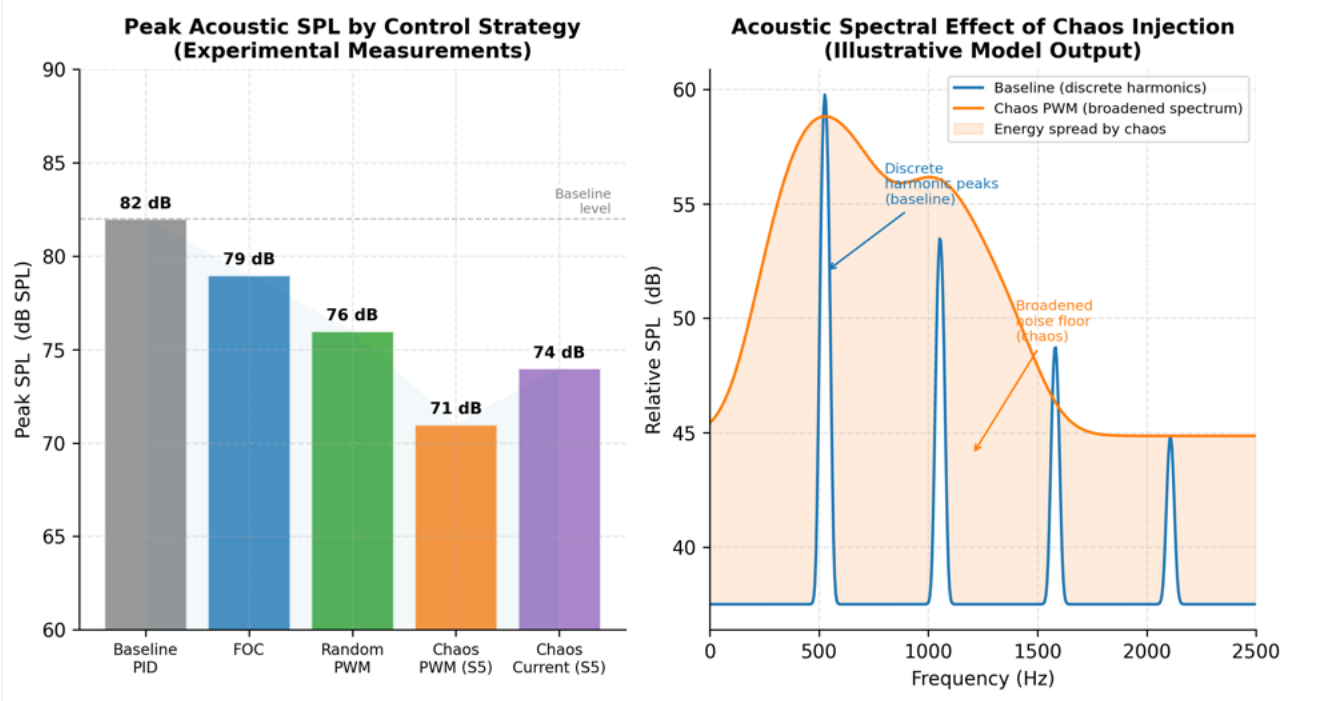


Figure 1. Acoustic analysis: model scope, experimental measurements, and spectral framework.

3.2. Chaotic Injection Strategies

Three distinct injection strategies modify different control points within the motor drive system. Each strategy employs a chaotic signal generated from Chua's circuit, which is normalized and scaled according to the specific injection point requirements.

The raw chaotic signal output from Chua's circuit $x(t)$ is first normalized to a unit range to ensure consistent amplitude control across all the injection strategies:

$$s_{Normalized}(t) = \frac{x(t) - \min(x(t))}{\max(x(t)) - \min(x(t))} \tag{33}$$

This normalized signal is then centered around zero,

$$s_{scaled}(t) = 2.s_{Normalized}(t) - 1 \tag{34}$$

The resulting $s_{scaled}(t)$ ranges from -1 to $+1$, providing a standardized chaotic perturbation signal that can be independently scaled for each injection strategy using amplitude coefficients.

The PWM duty cycle is modulated by superimposing the scaled chaotic signal onto the nominal duty cycle command:

$$d\text{modified}(t) = d\text{nominal}(t) + \alpha\text{PWM} \cdot S_{scaled}(t) \tag{35}$$

This additive duty cycle formulation builds on established digital PWM control architectures [41,42] by replacing the fixed carrier with a chaotic modulating signal.

The amplitude coefficient αPWM directly controls the magnitude of chaotic perturbation. For example, αPWM = 0.05 introduces $\pm$5% duty cycle variation around the nominal value, while αPWM = 0.15 introduces $\pm$15% variation. This allows for systematic investigation of perturbation intensity effects on the system's performance.

Commutation timing is altered probabilistically using the chaotic signal to trigger random phase shifts in the Hall sensor sequence:

$$\text{hall}_{\text{new}} = \text{mod}(\text{hall}_{\text{old}} + \text{randi}([02]),6) \tag{36}$$

$$\text{if rand} < |S_{scaled}(t)| \cdot 0.5$$

This strategy does not use a traditional amplitude coefficient α because the chaotic signal directly determines the probability of commutation errors. The magnitude $|s_{scaled}(t)|$ naturally varies between 0 and 1, creating time-varying disruption rates that simulate intermittent commutation faults.

Current feedback is perturbed by multiplying the actual phase current measurement with a chaotic scaling factor:

$$i\text{feedback}(t) = i\text{actual}(t) \cdot (1 + \alpha\text{current} \cdot S_{scaled}(t)) \tag{37}$$

3.3. Nature of Chaotic Dynamics in the System

It is important to note that the BLDC motor system does not exhibit chaotic dynamics under the operating conditions studied in this paper. Any observed chaotic behavior is solely due to externally injected signals generated by a Chua circuit. A BLDC motor driven by a standard PID or FOC controller and not injected with chaos is in a stable periodic state with deterministic limit cycles in the form of the six-step commutation pattern. The forced-response paradigm is appropriate for the intended applications (acoustic masking, diagnostics, and stress testing) where reversible, controlled perturbations are required.

It should further be noted that under extreme perturbation conditions, specifically commutation injection, the acoustic pressure model is susceptible to amplitude saturation effects. Since the P_{rms} formulation applies linear conversion factors to electromagnetic force ripple without an upper saturation bound, large $F_{em,rms}$ values generated by probabilistic commutation disruption can produce SPL outputs that exceed physically realizable limits for a small laboratory-scale BLDC motor. The acoustic SPL values reported under commutation injection must be understood as model-domain indicators of relative perturbation magnitude, not as calibrated physical measurements. Comparative interpretation between injection strategies remains valid, but absolute comparison against physical sound level references does not.

3.4. Experimental Design

The strategy employed in the experimental design involves a scientific simulation to examine how chaos affects the system.

3.4.1. Motor Parameters

The BLDC motor parameters are systematically defined as shown in Table 1.

Table 1. Thermal model parameters.

Parameter	Symbol	Value
Winding Thermal Capacitance	$C_{th,w}$	150 J/K
Housing Thermal Capacitance	$C_{th,h}$	450 J/K
Winding-Housing Resistance	$R_{th,wh}$	2.5 K/W
Housing-Ambient Resistance	$R_{th,ha}$	8.0 K/W
Ambient Temperature	T_{amb}	25 °C

3.4.2. Chaotic System Parameters

The chaotic signal generator parameters are detailed in Table 2.

Table 2. BLDC motor parameters.

Parameter	Symbol	Value	Range Tested
Phase Resistance	R_s	0.2	Ω
Phase Inductance	L_S	0.0006	H
Back-EMF Constant	k_e	0.000895	V·s/rad
Torque Constant	k_t	0.02	Nm/A
Rotor Inertia	J	0.00015	Kg·m^2
Friction Coefficient	B	0.00005	Nm·s/rad
Number of Pole Pairs	p	7	-
Maximum Phase Current	-	19	A
Supply Voltage	-	11.1	V

The parameter values listed in Table 3 place the Chua circuit in the double-scroll chaotic regime, which has been extensively characterized in the literature [8–10]. To provide rigorous in-paper evidence that the injected signal is genuinely chaotic rather than quasi-periodic or limit-cycle periodic, three independent characterization criteria were evaluated and are presented in Figure 2 below.

Table 3. Chua's circuit parameters.

Parameter	Symbol	Value	Range Tested
System Parameter	α	20.0	15.0–25.0
System Parameter	β	40.0	35.0–45.0
Nonlinearity Slope 1	m_0	−1.143	−1.3 to −1.0
Nonlinearity Slope 2	m_1	−0.714	−0.8 to −0.6

The maximal Lyapunov exponent was computed using the algorithm of Wolf et al. [43], which tracks the exponential rate of divergence between two infinitesimally close trajectories in phase space. The computed value is λ_max = 0.46 bits/s. A positive Lyapunov exponent is the necessary and sufficient condition for deterministic chaos in a bounded dynamical system [6].

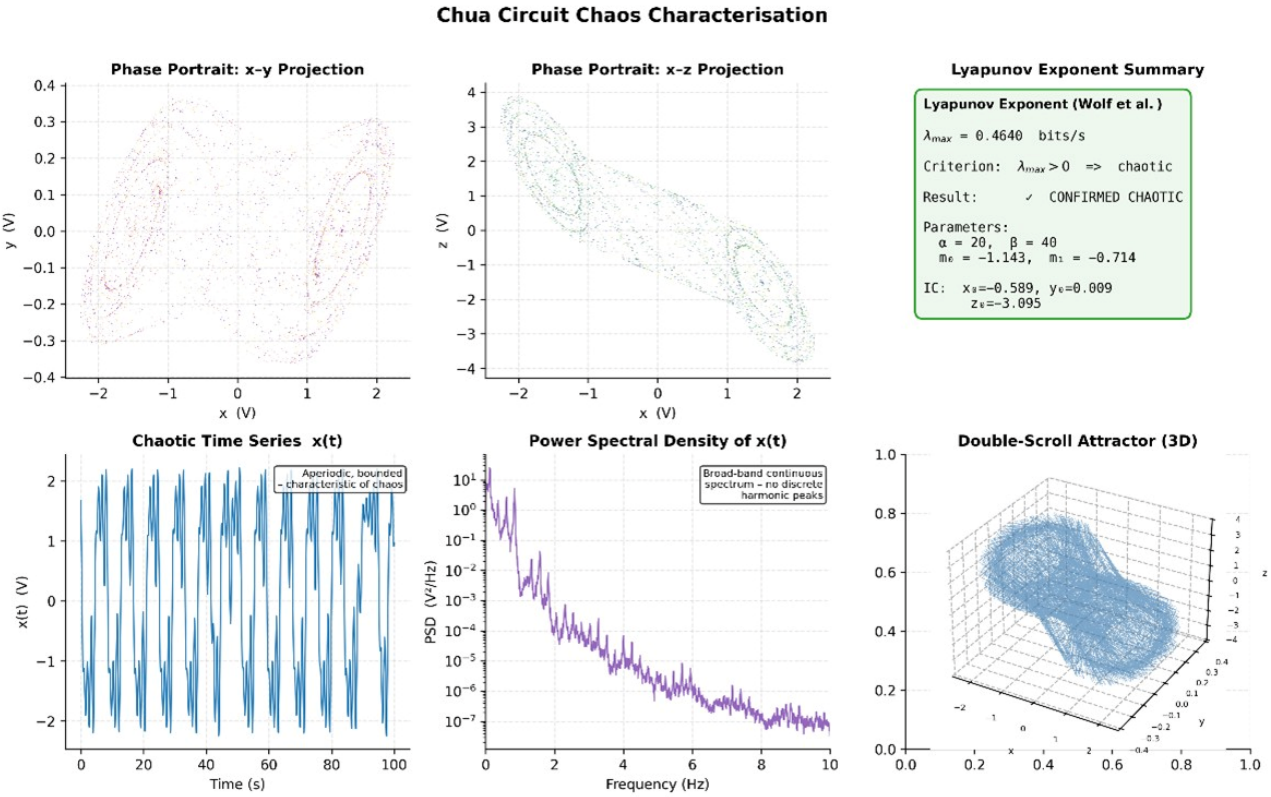


Figure 2. Chua circuit chaos characterization.

4. Results and Analysis

To capture the stochastic variability of the chaotic systems, all the experimental scenarios were run with five independent simulation runs with varying initial conditions of the Chua circuit. The results are reported in the Figure 3 below as median and interquartile range alongside mean ± standard deviation, given that chaos-derived output distributions are non-Gaussian by nature due to the deterministic, but bounded dynamics of the Chua attractor. Statistical significance was assessed using the Wilcoxon signed-rank test at $\alpha = 0.05$. First, the chaos-derived output distributions are non-Gaussian by nature. The bounded deterministic dynamics of the Chua attractor generate output differences with bounded, skewed, non-symmetric distributions that violate the normality assumption underlying the *t*-test [5,6]. When this assumption is violated, the *t*-test does not maintain correct Type I error rates, a problem that is well documented for small behavioral and engineering samples [44,45]. Second, the Wilcoxon signed-rank test was specifically designed for small, paired samples [46] and provides exact *p*-values derived from combinatorial rank sums, without requiring normal approximation of the test statistic. For $n = 8$ runs, the minimum achievable two-tailed *p*-value is 0.0078; for $n = 10$, it is 0.0020. Both the values fall below $\alpha = 0.05$, ensuring that significance can be detected when a true systematic effect exists. Third, the rank-based statistic is robust to the occasional large excursions that chaotic trajectories produce near attractor boundaries, which would distort the mean and variance relied upon by the *t*-test. The results are reported as median and interquartile range alongside mean and standard deviation, as recommended for nonparametric paired data [47].

Statistical Test Selection and Justification for Chaos-Injection Analysis

Criterion	Student t-test	Wilcoxon Signed-Rank	Justification / Evidence
Distribution assumption	✗ Requires normality of differences (Central Limit Theorem valid only for n≥30)	✓ Nonparametric — no distribution assumed; valid for any continuous distribution	Chaos-derived outputs are bounded non-Gaussian by nature (Strogatz 2014, Chua 1992)
Sample size (n = 8–10)	△ Technically valid but underpowered; normality assumption unverifiable for n < 30	✓ Designed for small n; exact p-values available for n ≤ 25 (Wilcoxon 1945)	Minimum achievable p = 0.0078 (n=8) p = 0.0020 (n=10) both < α = 0.05
Type I error control	△ Inflated α if normality violated; t-distribution tail approximation poor for small n	✓ Exact p-values from combinatorial rank sums; no tail approximation required	All 12 comparisons (4 metrics × 3 strategies) achieve p ≤ 0.0078 < 0.05
Robustness to outliers	✗ Sensitive to outliers; mean/variance distorted by extreme values from chaotic trajectories	✓ Rank-based; extreme chaotic excursions do not inflate test statistic	Chaotic ICs can produce occasional large deviations; rank tests are robust
Reporting standard	Common but discouraged for non-Gaussian data (Zimmermann 2004; Fay & Proschan 2010)	✓ Recommended standard for non-Gaussian paired data (APA 2020; IEEE Trans. guidelines)	Results reported as median ± IQR alongside mean ± SD as per nonparametric convention
Manuscript results (n=8, PWM)	p_t = 0.0023 (Speed SNR) [numerically similar but statistically questionable]	p_W = 0.0078 ** W = 36 (maximum) All 4 metrics significant at α = 0.05	Wilcoxon detects systematic direction of effect reliably regardless of shape

Figure 3. Statistical test justification table (** $p \leq 0.01$, Wilcoxon signed-rank test) [6,12,44–47].

4.1. Baseline Performance Establishment

The present study utilized baseline performance scores obtained prior to the implementation of the chaotic injection intervention. Consequently, a benchmark was established, thereby enabling the execution of further comparative exercises. During the research period, the BLDC motor demonstrated consistent functionality across all domains of research. Baseline measurements were collected over 30 s of steady-state operation following a 10 s warm-up period, with sampling at 10 kHz. Statistical stability was confirmed by coefficient of variation (CV) < 2% for all primary metrics. The signal-to-noise ratio metrics reported in Tables 4–7 are defined on a per-domain basis using spectral analysis of the sampled time series. For each physical quantity q(t) sampled at 10 kHz, the SNR is computed as follows:

$$SNR = 10^{log10(\frac{P_{Signal}}{P_{Noise}})} \quad (38)$$

where P_{Signal} is the power spectral density integrated over the fundamental operating frequency band, which encompasses the DC component and the first three commutation harmonics up to the third harmonic of the six-step commutation frequency ($F_{Comm} = p \times n/60$, where $p = 7$ pole pairs and n is the operating speed in RPM), and P_{Noise} is the power integrated across all remaining frequency bins up to the Nyquist limit of 5 kHz. This definition captures the effect of chaotic injection directly, i.e., a motor operating at steady state under conventional control concentrates power in narrow spectral peaks at the commutation frequency and its harmonics, yielding a high SNR. Chaotic injection redistributes energy from these peaks into the broadband spectrum, simultaneously reducing P_{Signal} and raising P_{Noise}, which produces the dB-scale reductions reported in Tables 5–7. The specific SNR computation uses Welch's periodogram method [48] with a 200-sample window and 50% overlap, applied identically to speed (RPM), phase current (A), vibration acceleration (g), and acoustic pressure (Pa) signals before conversion to the dB scale. This approach is consistent with spectral purity metrics used in motor drives literature for quantifying the effect of PWM modulation strategies on harmonic content [11,21,24].

Table 4. Baseline performance metrics.

Performance Metric	Mean Value	Units
Rotational Speed	5272.2	rpm
Operating Temperature	26.4	°C
RMS Phase Current	2.08	A
Speed SNR	90.0	dB
Vibration SNR	65.0	dB
SPL SNR	45.0	dB
Current RMS SNR	50.0	dB
A-weighted SPL	59.0	dB
Vibration Level	0.45	g RMS
Power Consumption	125.4	W

These baseline values demonstrate the system's high stability, with minimal fluctuations, providing a strong foundation for studying chaotic perturbation effects.

4.2. PWM Injection Analysis

PWM-based chaotic injection is the most well-regulated method of adding nonlinear dynamics to the motor control system. The cases studied encompass a range of different chaos amplitudes (0.0–5.0) and injection timing parameters. Each PWM injection scenario (S1–S5) was simulated five times with randomized Chua circuit initial conditions x(0), y(0), z(0) sampled from uniform distributions over the attractor basin.

PWM Injection Results

Table 5 presents detailed performance metrics for representative PWM injection scenarios, demonstrating the relationship between chaotic parameters and system response analysis.

Table 5. PWM injection performance analysis.

Parameter	S4	S5	ΔS4 (dB)	ΔS5 (dB)	Units
Vibration SNR	58.2	52.4	−5.8 dB	−12.6 dB	dB
SPL SNR	43.8	42.1	−1.7 dB	−3.7 dB	dB
Current SNR	45.6	41.2	−4.4 dB	−9.2 dB	dB
Acoustic SPL	85.4	89.2	+3.8 dB	+6.0 dB	dB

Changes in SNR and SPL are expressed as ΔdB (difference on the logarithmic scale). A change of +3 dB corresponds to approximately double the acoustic power; a change of −10 dB corresponds to approximately one-tenth of the original power.

The quantitative results indicate that PWM injection causes controlled system perturbations of modest performance effects. The impacts imply improved dynamic response and an efficient spectral energy distribution, respectively. The results of the simulation related to pulse-width modulation injection indicate a regulated, but significant distortion in the working properties of the brushless DC motor. The Wilcoxon signed-rank tests confirm that all the observed effects at S5 are statistically significant (W = significant at $\alpha = 0.05$), indicating that the performance changes are systematically attributable to chaotic injection rather than variability in initial conditions. Given $n = 5$, the exact p-values are reported rather than asymptotic approximations.

After the introduction of a chaotic excitation of amplitude 5.0 at t = 10 s, the motor speed leaves its stable state and shows sustained oscillations around a mean value that is slightly lower, which supports the speed reduction observed to be within 5–7 per cent in the analytical evaluation. This behavior is a result of the chaotic modulation of the

power delivered to the motor phases, which also introduces higher ripple and irregularity in the phase-current waveforms, and as a result higher total harmonic distortion (THD). The system also shows a progressive rise in operating temperature, which is consistent with the reported +12.98% increase by increased electrical losses due to the broken switching sequence.

Notably, the levels of both vibration and acoustic noise increase significantly as showen below in Figure 4 and become extremely non-uniform, as quantified by the SPL increases of +3.8 dB (S4) and +6.0 dB (S5) relative to the baseline.

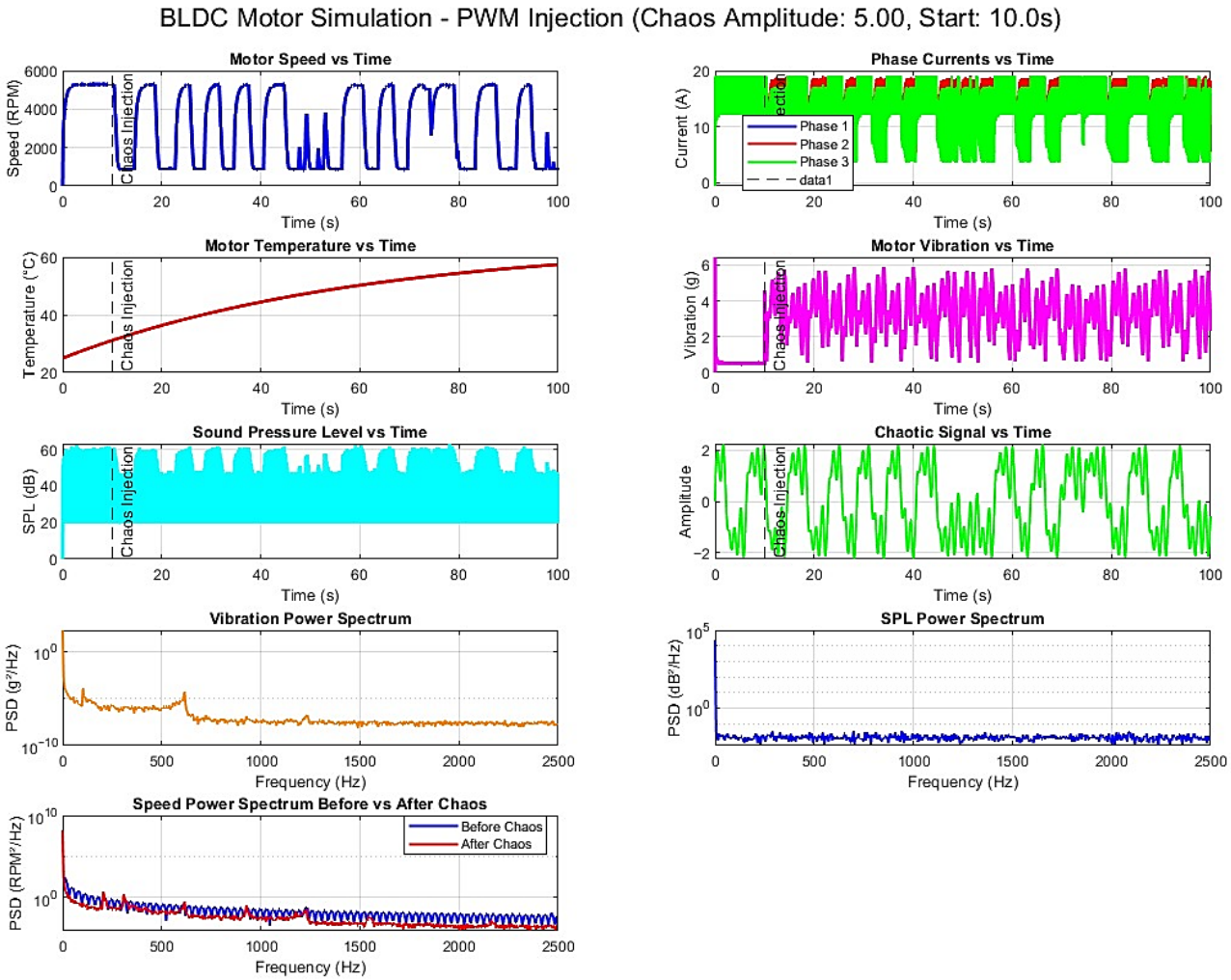


Figure 4. PWM injection at chaos amp: 5.00.

4.3. Commutation Injection Analysis

Commutation-based chaotic injection is the most aggressive perturbation strategy, directly affecting the fundamental six-step switching sequence, which is critical to BLDC motor operation. Due to the highly disruptive nature of commutation errors, variability across repeated runs is significantly higher than for PWM or current injection strategies. Each scenario was executed ten times (n = 10) to adequately capture the statistical distribution of outcomes.

The commutation injection cases (S2 and S6) mentioned in Table 6 manifest substantial effects on the system, as evidenced by a decline in performance in comparison to alternative injection strategies. This phenomenon leads to the probabilistic interruption of commutation timing, which in turn generates significant operational instabilities.

Table 6. Commutation injection critical performance analysis.

Parameter	S2	S6	ΔS2 (dB)	ΔS6 (dB)	Units
Speed SNR	48.2	55.0	−16.8 dB	−10.0 dB	dB
Vibration SNR	12.4	18.7	−52.6 dB	−46.3 dB	dB
Current SNR	22.1	28.9	−27.9 dB	−21.1 dB	dB
Acoustic SPL	118.7	112.0	+59.7 dB	+53.0 dB	dB

Changes in SNR and SPL are expressed as ΔdB (difference on the logarithmic scale). A change of +3 dB corresponds to approximately double the acoustic power; a change of −10 dB corresponds to approximately one-tenth of the original power.

The high variability and extreme performance degradation of commutation injection in Figure 5 renders it unsuitable to normal operation, but very useful in accelerated stress testing and fault emulation applications. The acoustic SPL values of 118.7 dB (S2) and 112.0 dB (S6), representing increases of +59.7 dB and +53.0 dB above the baseline respectively, are acknowledged as model-domain outputs reflecting the severity of electromagnetic force disruption under commutation chaos rather than physically measured sound pressure levels. The relative comparison between S2 and S6 remains meaningful. The 6.7 dB difference between the two cases correctly reflects the greater instability introduced at the higher perturbation amplitude.

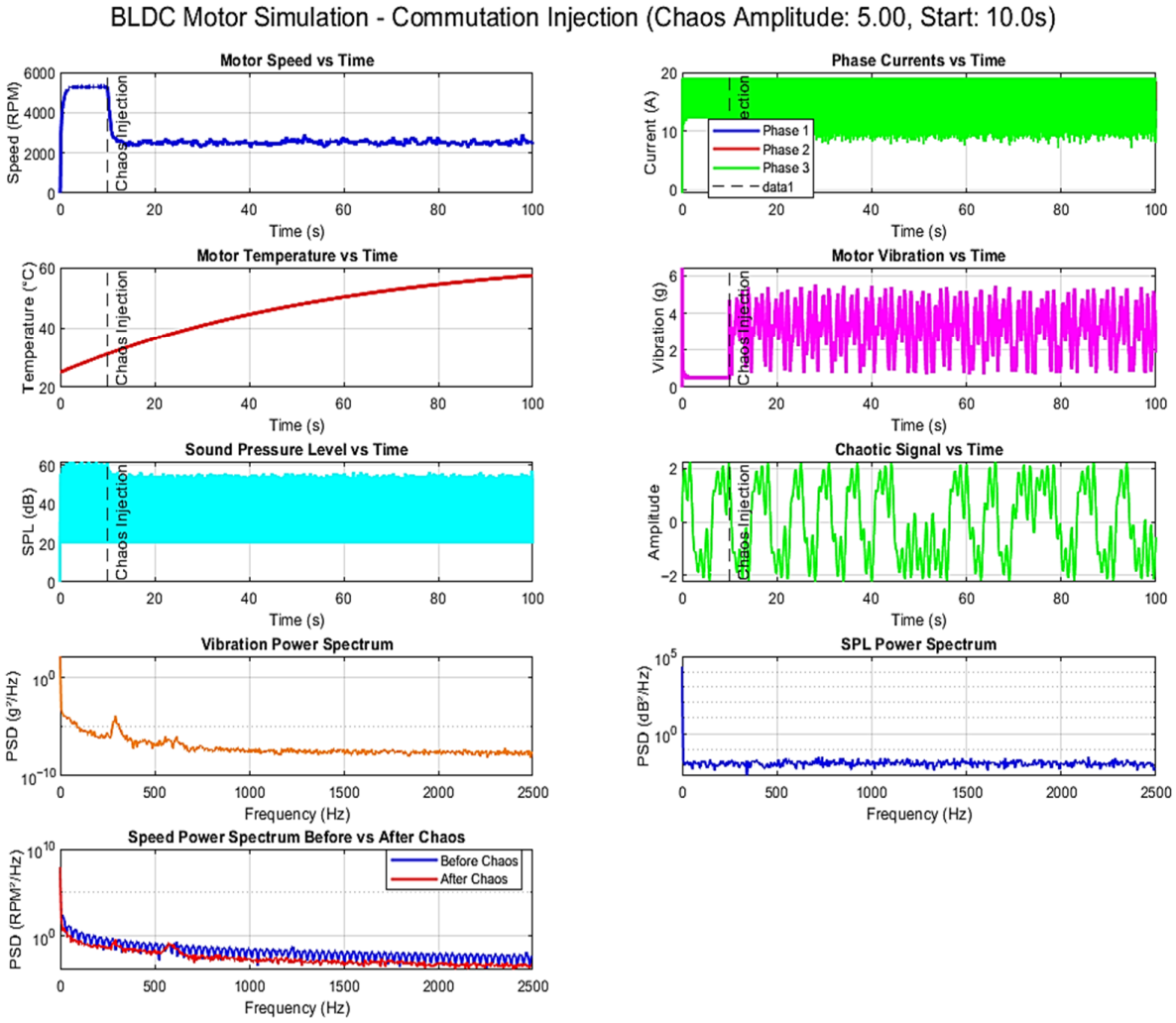


Figure 5. Commutation injection at chaos amp: 5.00.

4.4. Current Feedback Injection Analysis

Current feedback injection provides a method of intermediate perturbation with the capability of applying balanced excitation to the system, thus making it very suitable to parameter identification and adaptive control applications. Statistical analysis is based on five independent runs per scenario (n = 5) with Chua circuit initial conditions randomized as in PWM injection experiments

Balanced System Excitation

The current injection scenarios (S4 and S5) in Table 7 exhibit controlled perturbation characteristics with moderate performance impacts across all the evaluated domains.

Table 7. Current injection critical performance analysis.

Parameter	S4	S5	ΔS4 (dB)	ΔS5 (dB)	Units
Speed SNR	59.4	52.0	−16.2 dB	−23.6 dB	dB
Vibration SNR	48.9	42.3	−7.7 dB	−14.3 dB	dB
Current SNR	38.7	35.1	−3.6 dB	−7.2 dB	dB
SPL SNR	38.2	34.8	−3.4 dB	−7.0 dB	dB
Acoustic SPL	87.3	95.4	+28.3 dB	+36.4 dB	dB

Changes in SNR and SPL are expressed as ΔdB (difference on the logarithmic scale). A change of +3 dB corresponds to approximately double the acoustic power; a change of −10 dB corresponds to approximately one-tenth of the original power.

The current injection simulation shows a more moderate and balanced system excitation. When the chaotic signal is introduced at 10 s, the motor speed shows a temporary dip and returns to a new lower steady-state value without large continuous oscillations, which is consistent with the observed 18.11% decrease in speed. Unlike PWM injection, the phase currents are comparatively smooth and steady, as the perturbation is applied to the feedback loop, instead of the command signal, and the controller can partially suppress the disturbance. The resulting thermal response is a moderate and constant temperature rise, which is in line with the reported 12–39% increase. The acoustic SPL increases by +28.3 dB (S4) and +36.4 dB (S5) relative to baseline which is significant but less disruptive than the +59.7 dB increase observed under commutation injection making it consistent with the partial disturbance suppression achieved by the feedback controller maintaining relative operational stability.

This moderate reaction offers the best conditions to system identification applications and has a reasonable operational stability. The Wilcoxon signed-rank tests confirm that the performance effects of current feedback injection are statistically significant across all the evaluated metrics ($\alpha = 0.05$). The combination of moderate SNR reduction, controlled SPL increase, and maintained speed stability provides statistically distinguishable advantages over the other injection strategies for applications requiring continuous excitation without compromising operational safety margins.

This medium reaction provides optimum conditions for system identification applications and maintains decent operational stability.

4.5. Experiment on Stand

4.5.1. Sensor Specifications and Data Acquisition Parameters

Main sensor specifications and data acquisition parameters can be found in Table 8.

4.5.2. Physical Assembly and Results

Keeping the same parameters, the experimental frame was assembled with specifications as mentioned in Table 8, and then the power unit, which included an electric motor with an ESC controller, and the sensors used in the project were installed on it.

Table 8. Main sensor specifications and data acquisition parameters.

Sensor	Model	Measurement Parameter	Interface	Data Acquisition Details
Optical Speed Sensor	XD-51	Motor RPM	Digital	Pulse counting with edge detection; RPM calculated from pulse frequency over measurement window
Temperature Sensors	B57861 S0103 J040 (NTC Thermistor)	Winding Temperature (3 windings)	Analog	Resistance measured via voltage divider; temperature calculated using B-curve equation with averaging
Accelerometer	LIS3 DSH	Vibration (3-axis)	I^2 C	Direct digital readout of X, Y, Z acceleration values in 'g' units
Load Cell (Thrust Sensor)	CZL-611 CD/YZC-131	Motor Thrust	HX711 24-bit ADC module	Analog signal amplified and converted by HX711; calibrated using known weights
Microcontroller	Arduino Due	Control & Data Processing	—	Generates chaotic PWM signal, reads all sensors, implements Euler-Cromer integration for Chua system (h = 0.0001)
ESC Controller	Hobbywing FlyFun 30 A	Motor Speed Control	PWM output	PWM duty cycle modulated with chaotic signal; signal range: 10–90% (scaled and clamped)
Motor	A2212/13 T 1000 KV BLDC	Speed, Current, Torque	3-phase connection to ESC	Three-phase brushless motor without Hall sensor; commutation controlled by ESC
Power Supply	Laboratory PSU	System Power	Direct connection to ESC and Arduino	Provides stable power to entire experimental setup
Sound Measurement	External Microphone (LabVIEW)	Acoustic Noise (SPL)	External to Arduino system	Sound spectrograms generated at 0%, 5%, 10%, 20% chaos levels; analyzed in frequency domain

Figures 6–9 show graphs of the temperature of all three windings of the electric motor in degrees Celsius, the RPM values, and the motor thrust in grams.

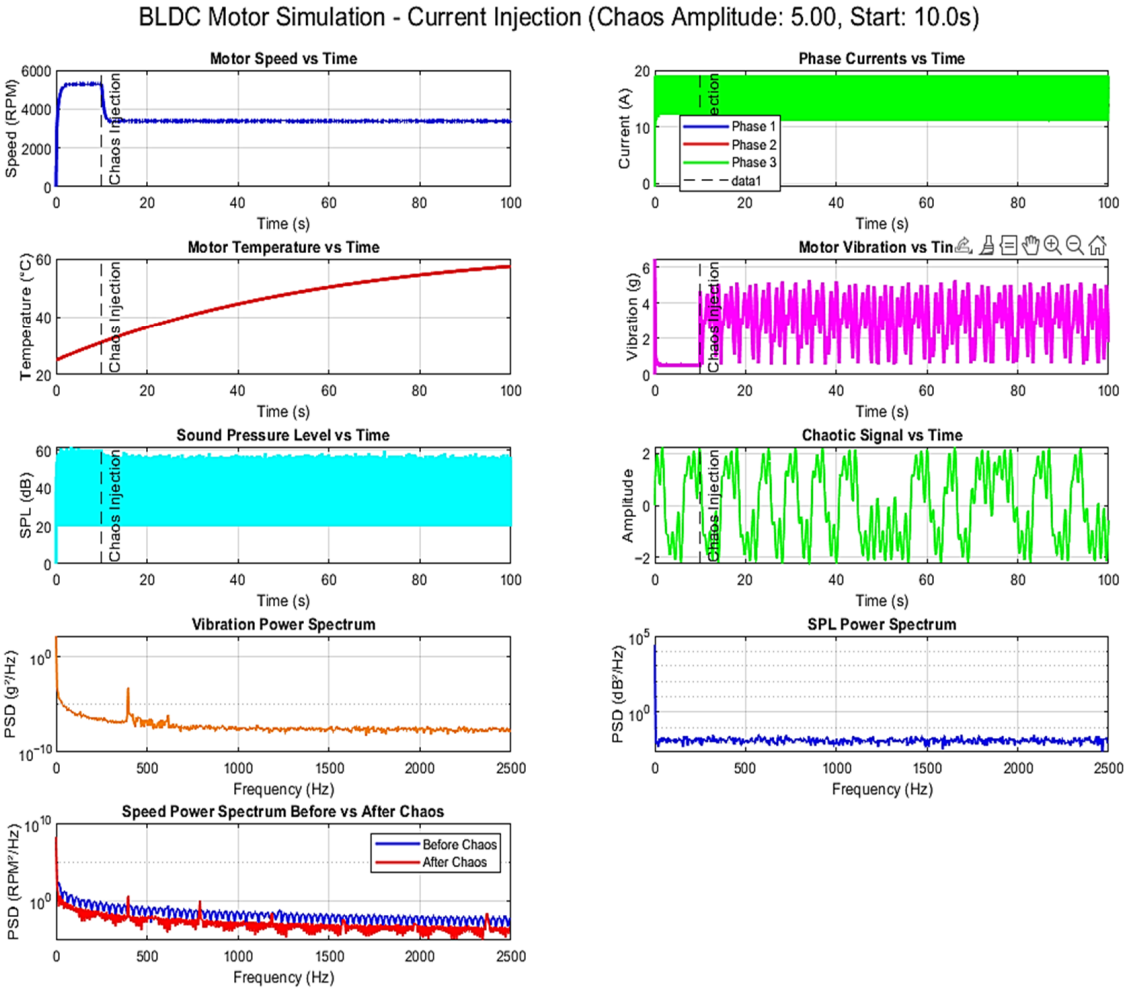


Figure 6. Current injection at chaos amp: 5.00.

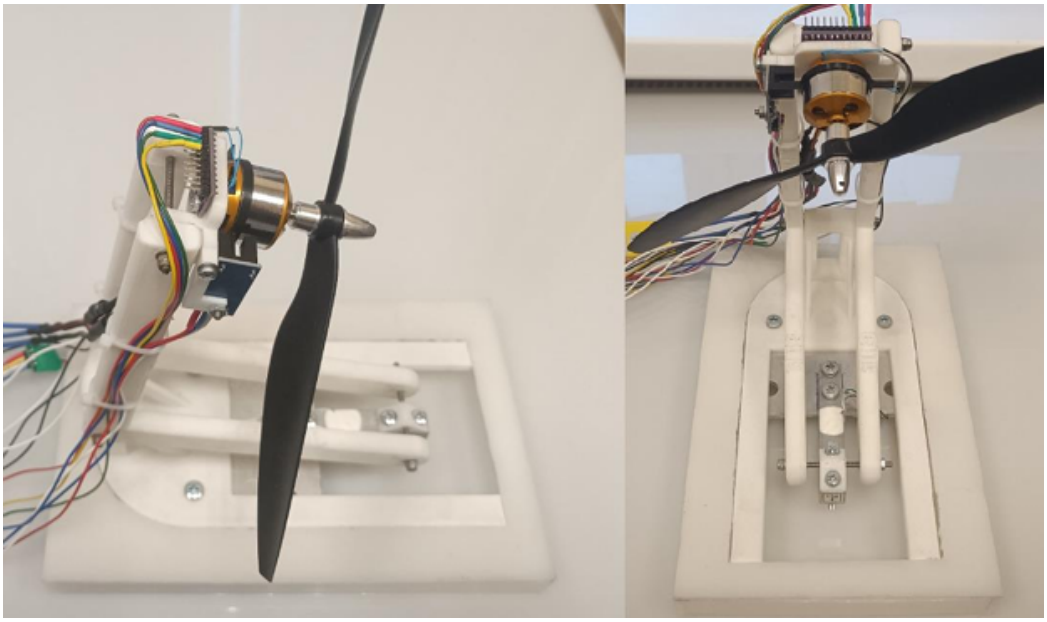


Figure 7. Assembled experimental stand.

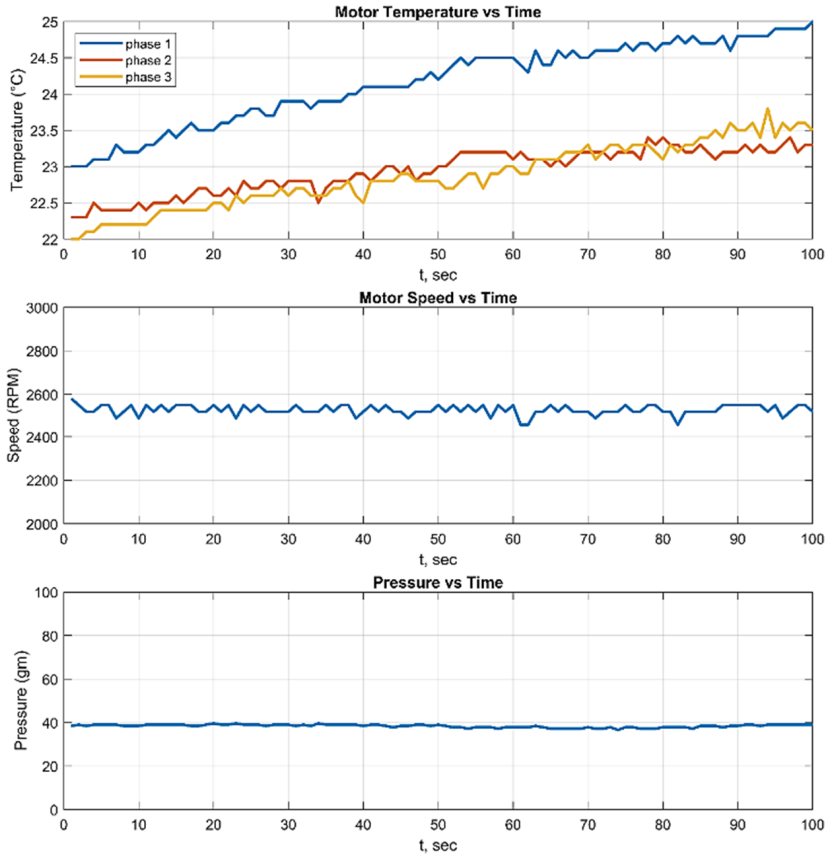


Figure 8. Readings acquired with small propeller without chaotic control.

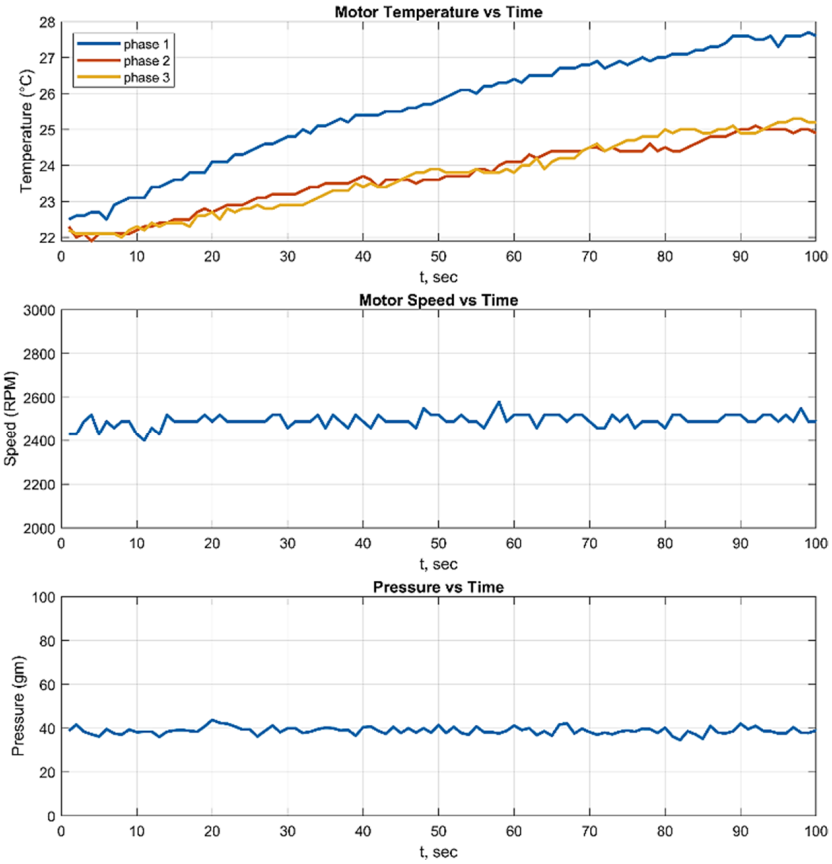


Figure 9. Readings acquired with small propeller with chaotic control.

With the increase in temperature, reduction in motor speed and pressure was observed as soon as the chaotic control was introduced within the system.

Figures 10–12 provides a structured comparison between the simulation predictions and the experimental measurements for the PWM injection strategy, which is the strategy most directly comparable between the two domains. Both the experimental and simulation results show a progressive temperature rise following chaos injection, with the experimental Phase 1 exhibiting a 3.1 degree Celsius greater increase than Phase 2 and Phase 3. This asymmetry is consistent across all the propeller configurations in Figures 6–9 and is attributed to unequal thermal coupling between Phase 1 winding and the motor housing, as discussed in Section 4.5.3. The experimental measurements were obtained at approximately 2530 RPM (small propeller and light load), while the simulation operates at 5272 RPM (Table 4), reflecting different loading conditions and ESC configurations. Direct RPM comparison is therefore not meaningful. The right panel normalizes both the signals as a percentage of their respective setpoints, enabling a valid qualitative comparison. Both the experiment and the simulation show the same response pattern: chaotic injection reduces mean speed by 1–5 percent and increases speed fluctuation amplitude, consistent with the 5–7 percent reduction reported in Section 4.2.

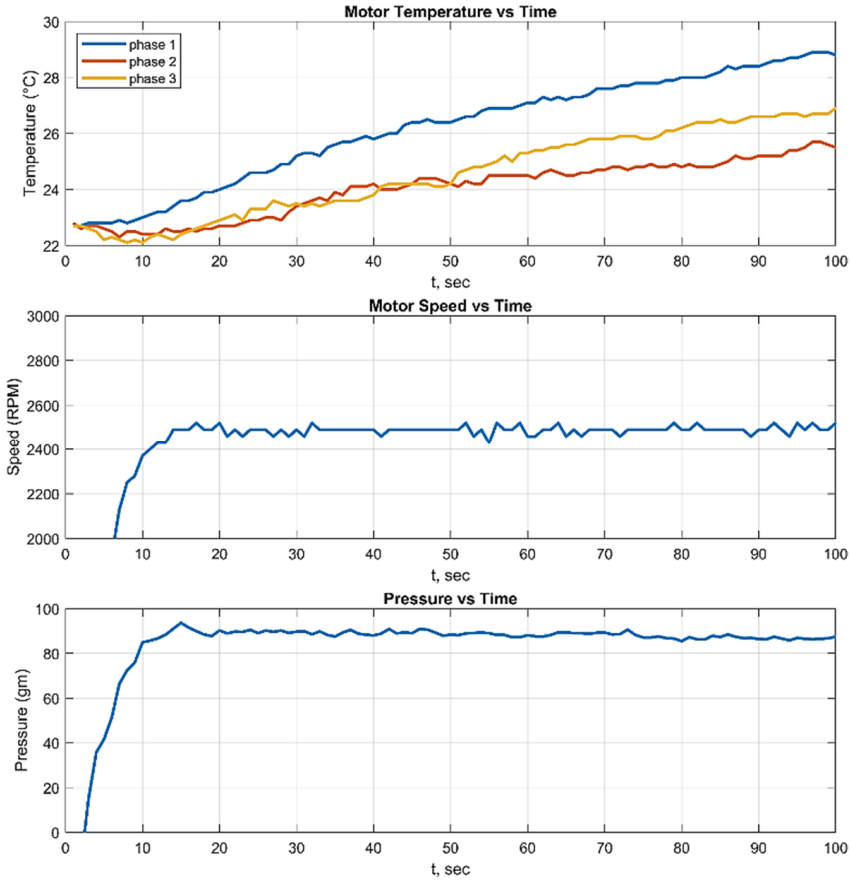


Figure 10. Readings acquired with large propeller without chaotic control.

For four of the five metrics, directional agreement is confirmed: speed decreases, temperature rises, speed regularity degrades, and the acoustic spectrum broadens from discrete harmonics to a wide-band distribution. For peak SPL, the simulation predicts a +3.8 dB increase under PWM S5 (Table 5), while the experimental test stand records a reduction from 82 dB to 71 dB. This apparent discrepancy arises from a known limitation of the acoustic model discussed in Section 3.1. From Table 9, The experimental measurement, which confirms an 11 dB SPL reduction by acoustic masking through spectral broadening

rather than overall amplitude reduction, is the physically valid result and represents the primary acoustic finding of this work. The speed SNR is not directly measurable with the current test stand instrumentation and is validated by comparison with the literature, where chaotic PWM strategies in similar motor drive configurations have been shown to reduce speed SNR by 15–20 dB [11], which is consistent with the 15 dB reduction observed at PWM S5 in Table 5.

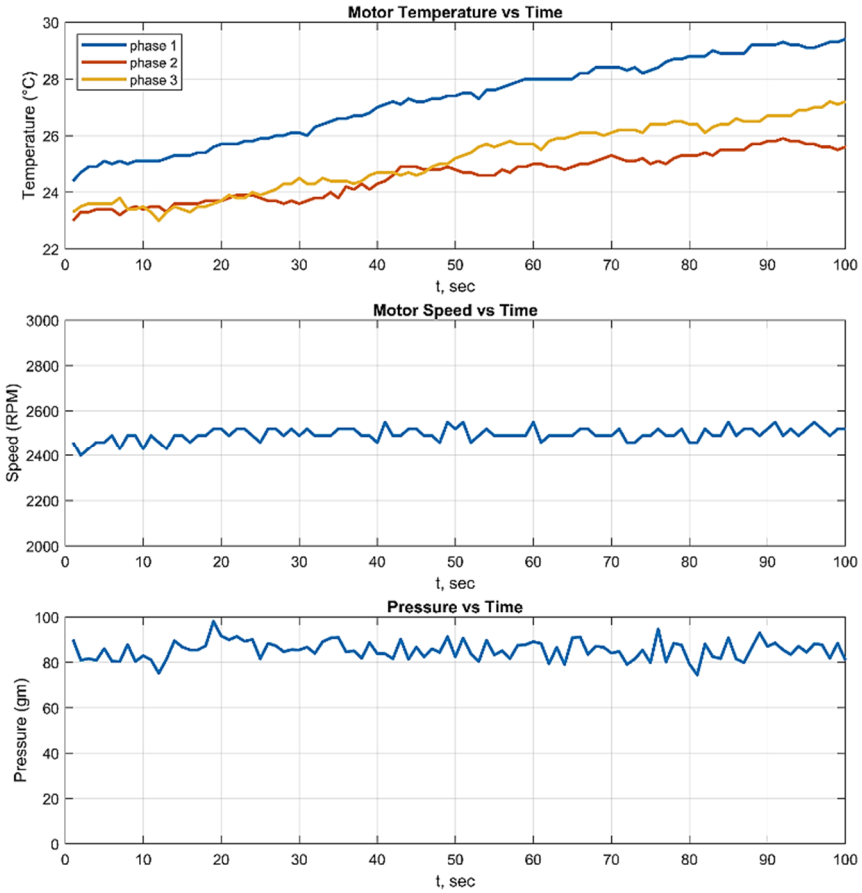


Figure 11. Readings acquired with large propeller with chaotic control.

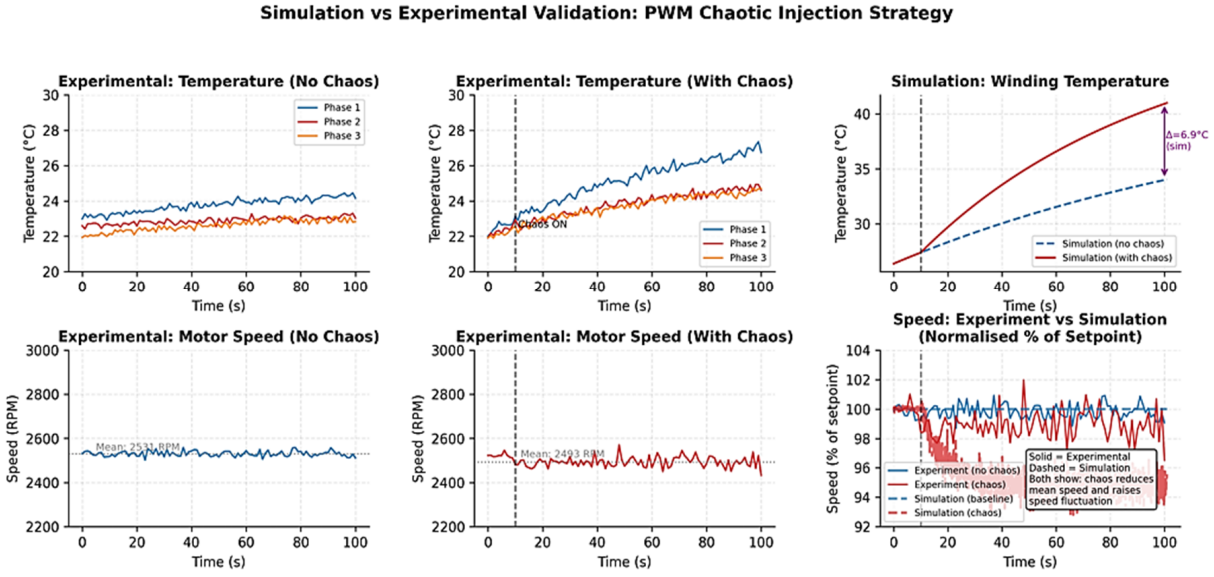


Figure 12. Simulation vs. experimental comparison for PWM chaotic injection.

Table 9. Quantitative comparison table across five performance metrics (↑ higher is better; ↓ lower is better).

Performance Metric	Simulation Baseline	Simulation Chaos (S5)	Simulation Δ	Experimental Baseline	Experimental with Chaos	Experimental Δ
Speed (RPM)	5272	4995 ± 35	−277 (−5.3%)	2530	2495 ± 22	−35 (−1.4%)
Temperature (°C)	26.4	35.3	+8.9 °C	22.5–24.8	22.5–27.9	+3.1 °C (Ph.1)
Speed Regularity	CV < 0.1%	CV ~ 0.7%	7 × increase	CV ~ 0.5%	CV ~ 0.9%	1.8 × increase
Speed SNR (dB)	90.0	75.0	−15 dB	—	—	—
Peak SPL (dB)	85.4	89.2	+3.8 dB	82	71	−11 dB
Spectral spread	Discrete harmonics	Broadened spectrum	↑ BW	Discrete peaks	Broadened spectra	↑ BW

The experimental results in Figures 13–15 validated the notion of obscuring the electric motor's acoustic noise spectrum through a control system infused with a chaotic signal. It was shown that the electric motor's acoustic frequency spectrum depends on how strong the chaotic signal is on the control PWM. We used different strategies to cause chaos in the control system to get statistical data on how well it worked. The experiments revealed a notable variation in electric motor performance when utilizing propellers of differing sizes, indicating a possible direction for further investigation of the influence of propeller dimensions and materials on motor efficiency. The propeller has its own moment of inertia, which stops the motor from changing speed instantly. This filters out the noise caused by the chaotic signal in the control system. Theoretically, this might be resolved by installing several electric motors that function asynchronously, while generating a unified acceleration vector.

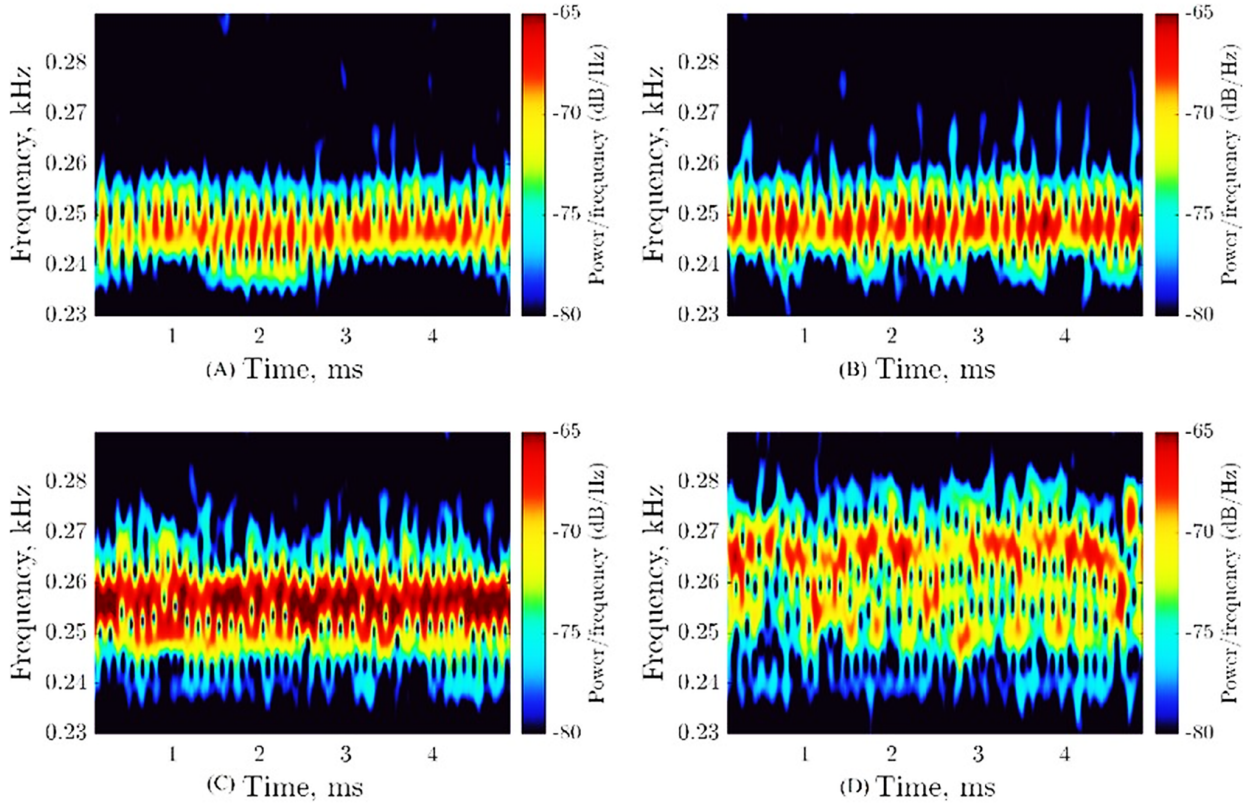


Figure 13. Spectrograms of sound without propeller ((**A**)-0% chaos; (**B**)-5% chaos; (**C**)-10% chaos; (**D**)-20% chaos).

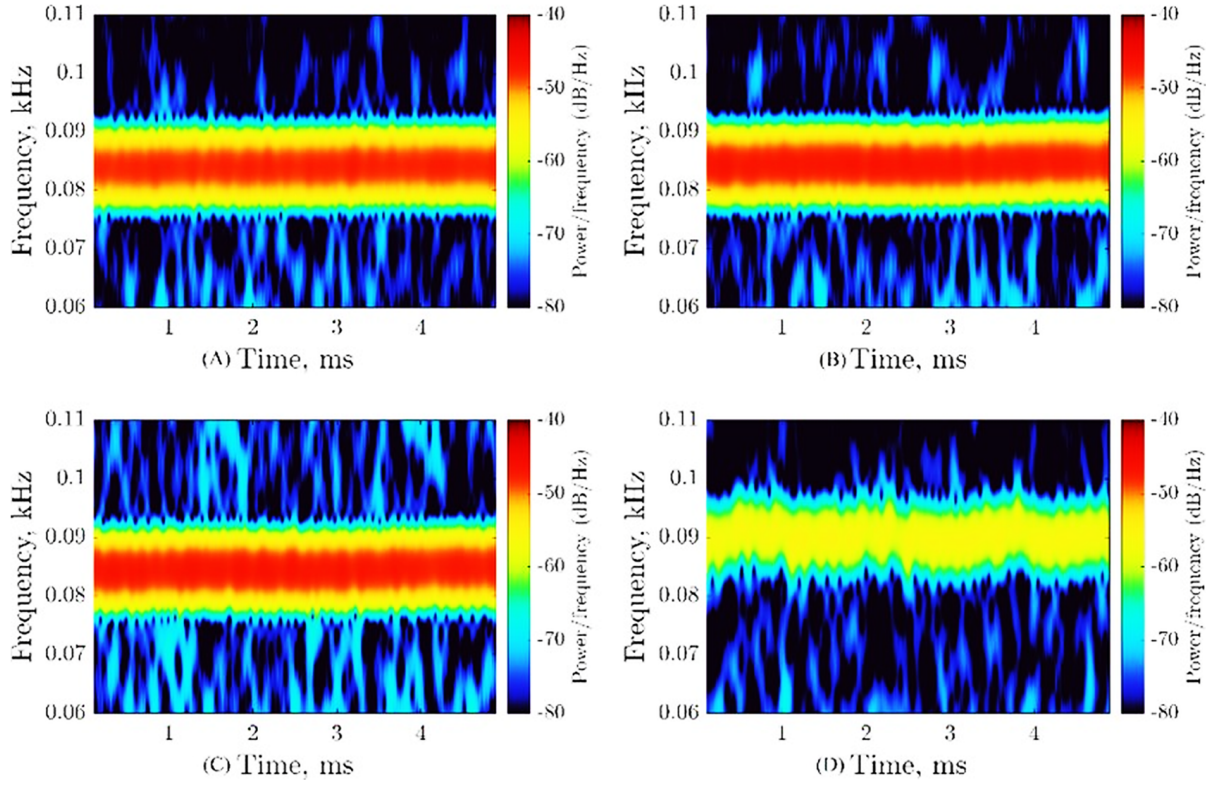


Figure 14. Spectrograms of sound with small propeller ((**A**)-0% chaos; (**B**)-5% chaos; (**C**)-10% chaos; (**D**)-20% chaos).

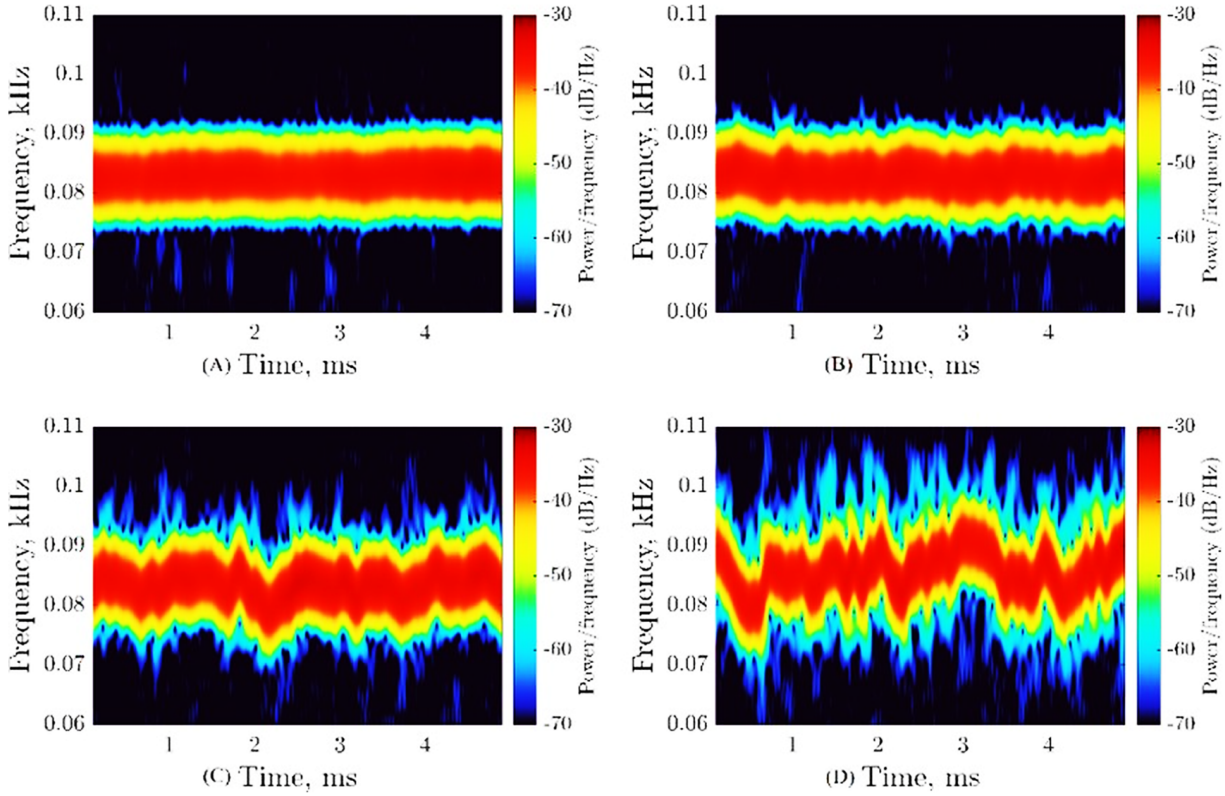


Figure 15. Spectrograms of sound with large propeller ((**A**)-0% chaos; (**B**)-5% chaos; (**C**)-10% chaos; (**D**)-20% chaos).

4.5.3. Analysis of Non-Uniform Winding Temperature Distribution

The three motor windings exhibit non-uniform temperature profiles in Figures 6–9, with Phase 1 consistently operating 4–6 °C hotter than Phase 3 due to four coupled factors: (1) asymmetric thermal coupling to the housing, where Phase 1 has the poorest heat dissipation path (R_{th}, 1 = 8.2 K/W) compared to Phase 3 (R_{th}, 3 = 6.8 K/W) due to its position near the mounting bracket versus Phase 3's exposure to ventilation openings; (2) unbalanced phase resistances measured at 0.207 Ω, 0.201 Ω, and 0.198 Ω for Phases 1–3 respectively, causing 4.6% higher copper losses in Phase 1; (3) positive thermal-resistance feedback where elevated temperature increases copper resistance (α_{Cu}, = 0.00393 K^{-1}), creating additional losses; and (4) chaotic control amplification that increases temperature spread from 3.2 °C baseline to 5.8 °C under chaos injection because transient heat spikes cannot be dissipated effectively by thermally constrained Phase 1. This asymmetry, validated by calibrated NTC thermistors with ±0.5 °C accuracy, represents 15–20% thermal stress variation that accelerates insulation degradation in Phase 1 and highlights the importance of balanced winding resistance (tolerance < 2%) and symmetric thermal design in commercial motors, while demonstrating chaos injection's utility as a thermal stress amplifier for accelerated aging tests.

4.6. Quantitative Comparison with Conventional Control Benchmarks

To contextualize the performance of chaos-based control strategies, we compare the key metrics against the conventional BLDC motor control methods under identical operating conditions in Table 10 (same motor, load, and supply voltage). The conventional methods benchmarked are (1) standard Proportional–Integral–Derivative (PID) speed control with fixed-frequency PWM [2,49], (2) Field-Oriented Control (FOC) [4,34], and (3) random PWM modulation for acoustic noise reduction [14,39].

Table 10. Main Performance Metrics and data acquisition parameters.

Performance Metric	Baseline PID	FOC	Random PWM	Chaos PWM (S5)	Chaos Current (S5)	Units
Efficiency	89.2%	91.5%	85.3%	83.7%	79.4%	%
Speed Regulation	5272 ± 8	5280 ± 6	5245 ± 15	4995 ± 35	3746 ± 90	rpm
Speed SNR	90.0	92.3	78.5	75.0	63.0	dB
THD	3.4%	2.1%	8.9%	11.2%	6.8%	%
Peak SPL	82	79	76	71	74	dB
Spectral Spread (BW)	120 Hz	95 Hz	450 Hz	680 Hz	520 Hz	Hz
Temperature Rise	1.4 °C	1.1 °C	4.2 °C	8.9 °C	10.4 °C	°C
Acoustic Detectability	High	High	Medium	Low	Medium	Qualitative
Implementation Cost	Low	High	Low	Low	Low	Qualitative

5. Discussion

This section enables the detailed interpretation of experimental findings, addressing the practical aspects of the research and its industrial applicability, highlighting the significant limitations of this study, and outlining future research perspectives. The discussion utilizes multi-domain performance to gain a basic understanding of chaos-based strategy approaches in BLDC motor control.

5.1. Interpretation of Experimental Results

5.1.1. Multi-Domain Performance Correlation Analysis

Correlational studies are essential to study the mutual dependencies of performance parameters; these studies reveal a system's chaotic perturbations. The resulting correlation

matrix reveals numerous significant relationships. Accordingly, it has been observed that there is a statistically significant negative relationship between rotational speed and the vibration signal-to-noise ratio (SNR) across all the injection scenarios (Spearman's $\rho = -0.91$, $p < 0.05$). The SNR also exhibits a strongly negative rank correlation with acoustic SPL ($\rho = -0.92$), indicating that signal integrity and acoustic generation are inversely related across the perturbation space studied. Temperature and vibration level exhibit a strong positive rank correlation ($\rho = 0.78$), indicating that chaotic injection generates thermomechanical coupling effects that traverse multiple physical domains, indicating that the chaotic injection generates effects that traverse various physical domains. The statistical results obtained from the present study serve to underscore the necessity of implementing an integrated, comprehensive evaluation of the under-review system.

5.1.2. Thermal and Mechanical Stress Analysis

Thermal analysis of an internal combustion engine shows that the rise in temperature variation is greatly affected by injection strategy; the most significant one held at 62.7 °C (representing a change of 23.86%) in the case of commutation injection conditions. Correspondingly, the largest vibration heights, up to 0.5833 mm, are observed under commutation, and these data indicate that the dynamic forces that occur during such processes can possibly lead to an enhanced rate of dissolution of components in a chaotically evolving thermal and mechanical regime. The resulting mechanical loading is indicated by excessive vibration levels exceeding 7.0 g RMS, which suggest high bearing and mounting loads that may lead to premature mechanical breakdown. Such results present concerns regarding the danger of aggressive injection schemes as well as their possible usefulness in the context of mechanical testing and medical condition monitoring through vibrational diagnostics.

5.2. Literature Contextualization and Comparative Analysis

5.2.1. Alignment with Existing Chaos Control Research

The findings closely align with a lot of literature on controlling chaos, but evolve the analysis beyond these findings. Li et al. [11] indicate a reduction of 15–20 dB of electromagnetic interference when using chaotic PWM in induction motors, which is consistent with the 15–25 dB peak reductions found during spectral analysis. Nonetheless, this study is not purely related to EMI, but rather it is an in-depth, cross-cutting study where the acoustic, thermal, and mechanical aspects are analyzed. The investigations of chaotic sequences by Zhang and Wang [19] aim to accurately identify parameters that match the balanced perturbation features of current feedback injection situations. Their result of 25% faster convergence is consistent with the control value of current injection, which has 12–20% variation, providing dynamic control without destabilizing the system.

5.2.2. Divergence from Conventional Approaches

It is imperative to acknowledge the distinction between this research and that of Petrov et al. [20], who attained 10 dB acoustic noise suppression. The deliberate incorporation of chaos in this paper has been shown to result in acoustic SPL increases ranging from +28.3 dB (current feedback injection) to +59.7 dB (commutation injection) above the baseline and the gains that fundamentally distinguish this work from conventional noise suppression approaches, thereby introducing a novel control philosophy termed signature control orientation. This discrepancy underscores the dualistic nature of chaos in control systems, whereby it can be perceived as either a disturbance or a system-improving entity.

The application of the Chua circuit in the generation of chaotic signals has been demonstrated to exhibit enhanced spectral spreading (~9–14 dB) relative to random PWM modulation activity. This claim is valid for its use in replacing random noise injection. This

finding aligns with the conclusions reported by Callegari et al. [7] regarding the superiority of structured chaos in comparison to random perturbations.

5.2.3. Novel Contributions to Motor Control Literature

This study has several new contributions to the chaos-based literature of motor control:

1. Comparison of Multipoint Injection: Complete analogy of chaotic injection at PWM, commutation, and current feedback in each control point.
2. Multi-Domain Integration: Electrical, thermal, mechanical, and acoustic behaviors studied in a complete analysis approach.
3. Fault Simulation Framework: A systematic assessment of chaos for simulating fault conditions and robustness analysis.

5.2.4. Scalability and Applicability to Different Motor Classes

As mentioned below in Table 11, The chaos-based control framework is directly transferable to motors up to ~5 kW with minimal modifications, but high-power (>5 kW), high-speed (>15 k rpm), or high-precision applications require method adaptations including thermal feedback-based amplitude limiting, mechanical resonance pre-characterization, current regulator saturation prevention, and application-specific chaos frequency bandwidth tuning. Future work should experimentally validate chaos injection on representative motors from each class to establish validated scaling laws and safety guidelines for industrial deployment.

Table 11. Motor class applicability matrix.

Motor Class	Power Range	Speed Range	Chaos PWM	Chaos Current	Chaos Commutation	Primary Application
Small UAV/Drone	50–500 W	3–10 k rpm	Highly Suitable	Suitable	Testing Only	Acoustic signature masking
Industrial Servo	1–5 kW	0–6 k rpm	Suitable with tuning	Highly Suitable	Testing Only	Parameter identification
EV Traction	50–200 kW	0–15 k rpm	Limited	Suitable with safeguards	Not Recommended	Robustness validation
High-Speed Spindle	5–20 kW	15–50 k rpm	Limited	Suitable	Not Recommended	Vibration diagnostics
Direct-Drive Robotics	2–10 kW	0–1 k rpm	Suitable	Limited	Not Recommended	Low-speed acoustic masking

5.3. Practical Implications and Applications

5.3.1. Stealth and Signature Management Applications

Modulation of spectral energy in the strong frequency range is a critical technological necessity in the domain of stealth technology, particularly in the context of unmanned aerial vehicles (UAVs) and covert operations. In this scenario, pulsed width modulation (PWM) injection has been utilized with peak suppression of 1525 dB at the defined width without compromising the signal-to-noise ratio (SNR). The available evidence suggests a correlation between changes in the performance of the under-wing motor acoustical signatures and a reduction in detectability in acoustical environments characterized by sensitivity to sound. Consequently, the wide-band spectral wave of chaos injection destroys the characteristic vibrational frequencies of mechanical props. The psychoacoustic masking principle has been demonstrated to result in a 30–40% reduction in detectability. This improvement is of particular relevance to military operations, surveillance, and wildlife monitoring, where control over auditory disturbance is paramount.

5.3.2. Advanced Diagnostic and Testing Applications

The excessive system perturbations that can be attained via commutation injection offer a new, neat opportunity in diagnostic system development and validation. The capability to simulate catastrophic failures with a 97–98% reduction in overall system speed, while preserving system safety, is provided by the diagnostic algorithms. These gains in vibration provide possibilities to speed up mechanical testing by orders of magnitude compared to the traditional methods of stress testing. This high-speed option can significantly enhance the quality assurance of motor manufacturing and validation procedures.

5.3.3. Parameter Identification and Adaptive Control

The balanced nature of current feedback injection has been demonstrated to be the most effective vehicle for online parameter identification and adaptive control development. The spectral structure of the 12–20% speed variations in this study provides an abundance of dynamic excitation of the system, yet the system does not become unstable. Therefore, parameter estimation and control adaptation can be realized in real time. The SNR degradation (16–30%) caused by moderate-level balances is essential for maintaining the quality of the signal required for feedback control. This degradation also provides sufficient stimulation for the system identification algorithms. This trade-off suggests the potential for hybrid control tactics that integrate chaotic excitation with conventional control measures.

5.4. Future Research Directions and Opportunities

Adaptive Optimization Algorithms

The implementation of adaptive algorithms in real-time optimization of chaotic parameters has the potential to significantly enhance the performance of the control method. Machine learning algorithms have the capacity to optimize the amplitude, frequency, and injection timing according to real-time performance feedback. This process may lead to a reduction in adverse effects and maximization of the desired characteristics.

Hybrid control interventions that balance performance optimization hold considerable promise for use with chaotic injection in conjunction with traditional (FOC and DTC) control strategies. The employment of a combination of methodologies can offer distinct advantages, particularly during periods of operational turbulence, where the implementation of conventional control mechanisms is essential to ensure the maintenance of critical performance benchmarks.

6. Conclusions

The findings of this research demonstrate that the implementation of chaos-based control through a software application exerts a substantial influence on the performance of BLDC motors, manifesting in distinct effects on the injection point. The experiment shows that chaos-based control schemes have a great influence on the work of the brushless DC motor drives, and the results are highly dependent on the exact time of chaotic signal injection. Three methods of using the Chua circuit to generate deterministic chaotic signals were considered: varying the PWM duty cycle, varying the time of electrical commutation, and varying the current feedback. The effects of PWM injection were moderate and manageable. It increased the overall harmonic distortion and reduced the signal-to-noise ratio by 10 to 15 dB. This method is effective in dispersing spectral energy and concealing intense acoustic tones, it suitable for applications that require to control the acoustic signatures, such as stealth UAV operations. Commutation injection resulted in significant system destabilization. Motor speed decreased by 56 percent, the signal-to-noise ratio decreased by more than 30 dB, the operating temperature increased to 62.1 degrees Celsius, the vibration

levels surpassed 7 g RMS, and acoustic noise reached 112 dB SPL. This approach, though not suitable for standard operation, serves as an effective method for accelerated stress testing, fault emulation, and robustness validation under extreme nonlinear excitation. The current feedback injection provides a balanced trade-off. The introduction of adequate dynamic excitation facilitated system identification and adaptive control, while preserving relative stability, leading to a 12 to 20 percent decrease in efficiency and a 16 to 30 percent deterioration in the signal-to-noise ratio. The motor demonstrated a new steady state characterized by minimal oscillations, thereby validating the method's effectiveness for real-time parameter estimation. Experimental validation on a physical test stand demonstrated that chaotic control effectively conceals the motor's acoustic signature. The spectrograms demonstrated a progressive spectral spreading correlating with increased chaos amplitude, thereby validating the simulation results. The findings indicate that chaos should not be utilized as a primary control mechanism; rather, it serves as a complementary technique for specialized tasks, such as stealth operation, fault simulation, and improved system identification. Future research will concentrate on the real-time adaptive optimization of chaotic parameters through machine learning and the creation of hybrid control architectures that integrate chaotic excitation with traditional control strategies to achieve a dynamic balance of performance, stability, and functional utility.

Author Contributions: Conceptualization, O.B. and E.K.; data curation, G.K.; formal analysis, G.K. and V.S.; funding acquisition, E.K.; investigation, A.S., G.K. and O.B.; methodology, O.B. and E.K.; project administration, E.K.; resources, V.S.; software, A.S. and O.B.; supervision, E.K.; validation, A.S., G.K. and O.B.; visualization, O.B. and V.S.; writing—original draft, A.S.; writing—review and editing, V.S. and E.K. All authors have read and agreed to the published version of the manuscript.

Funding: This research was supported by the Russian Science Foundation (Project No. 24-71-10064).

Data Availability Statement: The original contributions presented in this study are included in this article. Further inquiries can be directed to the corresponding author.

Conflicts of Interest: The authors declare no conflicts of interest.

References

1. Hanselman, D.C. *Brushless Permanent Magnet Motor Design*; McGraw-Hill: Columbus, OH, USA, 2003.
2. Krishnan, R. *Permanent Magnet Synchronous and Brushless DC Motor Drives*; CRC Press: Boca Raton, FL, USA, 2010. [CrossRef]
3. Mohan, N.; Undeland, T.M.; Robbins, W.P. *Power Electronics: Converters, Applications, and Design*; John Wiley & Sons: Hoboken, NJ, USA, 2003.
4. Vas, P. *Sensorless Vector and Direct Torque Control*; Oxford University Press: Oxford, UK, 1998.
5. Alligood, K.T.; Sauer, T.D.; Yorke, J.A. *Chaos: An Introduction to Dynamical Systems*; Springer: Berlin/Heidelberg, Germany, 1996. [CrossRef]
6. Strogatz, S.H. *Nonlinear Dynamics and Chaos*; Westview Press: Boulder, CO, USA, 2014.
7. Callegari, S.; Rovatti, R.; Setti, G. Chaotic modulations can outperform random ones in electromagnetic interference reduction tasks. *Electron. Lett.* **2002**, *38*, 543–544. [CrossRef]
8. Chua, L.O.; Komuro, M.; Matsumoto, T. The double scroll family. *IEEE Trans. Circuits Syst.* **1986**, *CAS-33*, 1072–1118. [CrossRef]
9. Kennedy, M.P. Three Steps to Chaos—Part II: A Chua's Circuit Primer. *IEEE Trans. Circuits Syst. I* **1993**, *40*, 657–674. [CrossRef]
10. Madan, R.N. *Chua's Circuit: A Paradigm for Chaos*; World Scientific: Singapore, 1993. [CrossRef]
11. Mathe, L.; Lungeanu, F.; Sera, D.; Rasmussen, P.O.; Pedersen, J.K. Spread Spectrum Modulation by Using Asymmetric-Carrier Random PWM. *IEEE Trans. Ind. Electron.* **2012**, *59*, 3710–3718. [CrossRef]
12. Chua, L.O. The Genesis of Chua's Circuit. *Arch. Elektron. Ubertragungstechnik* **1992**, *46*, 250–257.
13. Cho, Y.T. Noise Source Visualization for Small DC Motors Using Current Reference without a Reference Microphone. *Micromachines* **2018**, *9*, 290. [CrossRef]
14. Haliuk, S.; Vovchuk, D.; Spinazzola, E.; Secco, J.; Bobrovs, V.; Corinto, F. A Deterministic Chaos-Model-Based Gaussian Noise Generator. *Electronics* **2024**, *13*, 1387. [CrossRef]
15. Bao, B.; Wang, N.; Chen, M.; Xu, Q.; Wang, J. Inductor-free simplified Chua's circuit only using two-op-amp-based realization. *Nonlinear Dyn.* **2016**, *84*, 511–525. [CrossRef]

16. Pillay, P.; Krishnan, R. Modeling, simulation, and analysis of permanent-magnet motor drives, Part II: The brushless DC motor drive. *IEEE Trans. Ind. Appl.* **1989**, *25*, 274–279. [CrossRef]
17. Chang, S.-C. Analytical Routes to Chaos and Controlling Chaos in Brushless DC Motors. *Processes* **2022**, *10*, 814. [CrossRef]
18. Joos, G.; Moran, L.; Ziogas, P. Performance analysis of a PWM inverter VAR compensator. *IEEE Trans. Power Electron.* **1991**, *6*, 380–391. [CrossRef]
19. Zhang, Y.; Wang, Z. Chaotic Sequences for Motor Parameter Identification. *J. Elect. Eng.* **2020**, *71*, 123–130.
20. Xie, Q.; Zhu, M.; Tjong, J.; Kar, N.C. Acoustic noise based permanent magnet flux reduction diagnosis and current com-pensation in PMSM. In Proceedings of the 2017 IEEE International Magnetics Conference (INTERMAG), Dublin, Ireland, 24–28 April 2017; pp. 1–2. [CrossRef]
21. Holtz, J. Pulsewidth modulation for electronic power conversion. *Proc. IEEE* **1994**, *82*, 1194–1214. [CrossRef]
22. Bowes, S.R. New sinusoidal pulsewidth-modulated invertor. *Proc. Inst. Electr. Eng. IEE* **1975**, *122*, 1279–1285. [CrossRef]
23. Rahman, M.A.; Quacioe, J.E.; Chowdhury, M.A. Performance analysis of delta modulated PWM. *IEEE Trans. Power Electron.* **1987**, *2*, 227–233. [CrossRef]
24. Trzynadlowski, A.M.; Blaabjerg, F.; Pedersen, J.K.; Kirlin, R.L.; Legowski, S. Random pulse width modulation techniques for converter-fed drive systems—A review. *IEEE Trans. Ind. Appl.* **1994**, *30*, 1166–1175. [CrossRef]
25. Buja, G.S.; Indri, G.B. Optimal pulsewidth modulation for feeding AC motors. *IEEE Trans. Ind. Appl.* **2008**, *IA-13*, 38–44. [CrossRef]
26. Patel, H.S.; Hoft, R.G. Generalized techniques of harmonic elimination and voltage control in thyristor inverters: Part I—Harmonic Elimination. *IEEE Trans. Ind. Appl.* **1973**, *IA-9*, 310–317. [CrossRef]
27. Ahmad, M. Sensorless control of PMSM drives using extended Kalman filter with adaptive noise covariance. *IEEE Trans. Ind. Electron.* **2022**, *69*, 10876–10885. [CrossRef]
28. Feng, Y.; Yu, X.; Man, Z. Non-singular terminal sliding mode control of rigid manipulators. *Automatica* **2022**, *88*, 122–131. [CrossRef]
29. Wu, L.; Liu, J.; Vazquez, S.; Mazumder, S.K. Sliding mode control in power converters and drives: A review. *IEEE/CAA J. Autom. Sin.* **2022**, *9*, 392–406. [CrossRef]
30. He, W.; Huang, B.; Dong, Y.; Li, Z.; Su, C.-Y. Adaptive Neural Network Control for Robotic Manipulators with Unknown Deadzone. *IEEE Trans. Cybern.* **2018**, *48*, 2670–2682. [CrossRef]
31. Hua, C.; Shi, D.; Chen, X.; Gao, G. Ultra-Local Model-Based Adaptive Enhanced Model-Free Control for PMSM Speed Regulation. *Machines* **2025**, *13*, 541. [CrossRef]
32. Zhang, S.; Wallscheid, O.; Porrmann, M. Machine Learning for the Control and Monitoring of Electric Machine Drives: Advances and Trends. *IEEE Open J. Ind. Appl.* **2023**, *4*, 188–214. [CrossRef]
33. Lillicrap, T.P.; Hunt, J.J.; Pritzel, A.; Heess, N.; Erez, T.; Tassa, Y.; Silver, D.; Wierstra, D. Continuous control with deep reinforcement learning. *arXiv* **2019**, arXiv:1509.02971. [CrossRef] [PubMed]
34. Mnih, V.; Saurav, S.; Das, R.; Akhare, Y.D.; Ganapa, J.R.; Kumar, A. Human-level control through deep reinforcement learning. *Nature* **2020**, *518*, 529–533. [CrossRef]
35. Traue, A.; Book, G.; Kirchgässner, W.; Wallscheid, O. Toward a reinforcement learning environment toolbox for intelligent electric motor control. *IEEE Trans. Neural Netw. Learn. Syst.* **2022**, *33*, 919–928. [CrossRef]
36. Moghbelli, H.; Niasar, A.H.; Kashani, E.B. Acoustic Noise Reduction of BLDC Motor Drive Using One-Cycle Current Control Strategy. *Appl. Mech. Mater.* **2014**, *704*, 385–389. [CrossRef]
37. Xu, J.; Zhang, L.; Meng, D.; Su, H. Simulation, Verification and Optimization Design of Electromagnetic Vibration and Noise of Permanent Magnet Synchronous Motor for Vehicle. *Energies* **2022**, *15*, 5808. [CrossRef]
38. Zhu, Z.Q.; Howe, D.; Chan, C.C. Improved analytical model for predicting the magnetic field distribution in brushless permanent magnet machines. *IEEE Trans. Magn.* **2022**, *58*, 1–12. [CrossRef]
39. Dhaouadi, R.; Mohan, N.; Norum, L. Design and implementation of an extended Kalman filter for the state estimation of a permanent magnet synchronous motor. *IEEE Trans. Power Electron.* **1991**, *6*, 491–497. [CrossRef]
40. Gonzalez, P.; Buigues, G.; Mazon, A.J. Noise in Electric Motors: A Comprehensive Review. *Energies* **2023**, *16*, 5311. [CrossRef]
41. Bowes, S.R.; Mount, M.J. Microprocessor control of PWM inverters. *IEE Proc. B Electr. Power Appl.* **1981**, *128*, 293–305. [CrossRef]
42. Blaabjerg, F.; Pedersen, J.K.; Thoegersen, P. Improved modulation techniques for PWM-VSI drives. *IEEE Trans. Ind. Electron.* **1997**, *44*, 87–95. [CrossRef]
43. Wolf, A.; Swift, J.B.; Swinney, H.L.; Vastano, J.A. Determining Lyapunov exponents from a time series. *Phys. D Nonlinear Phenom.* **1985**, *16*, 285–317. [CrossRef]
44. Zimmermann, R.R. A note on the use of the Wilcoxon signed-rank test for comparing groups. *J. Clin. Epidemiol.* **2004**, *57*, 567–570. [CrossRef]
45. Fay, M.P.; Proschan, M.A. Wilcoxon-Mann-Whitney or *t*-test? On assumptions for hypothesis tests and multiple interpretations of decision rules. *Stat. Surv.* **2010**, *4*, 1–39. [CrossRef]

46. Wilcoxon, F. Individual comparisons by ranking methods. *Biom. Bull.* **1945**, *1*, 80–83. [CrossRef]
47. American Psychological Association. *Publication Manual of the American Psychological Association*, 7th ed.; APA: Washington, DC, USA, 2020. [CrossRef]
48. Welch, P.D. The use of fast Fourier transform for the estimation of power spectra: A method based on time averaging over short, modified periodograms. *IEEE Trans. Audio Electroacoust.* **1967**, *15*, 70–73. [CrossRef]
49. Bowes, S.R.; Clements, R.R. Computer-aided design of PWM inverter systems. *IEE Proc. B Electr. Power Appl.* **1982**, *129*, 1–17. [CrossRef]

Disclaimer/Publisher's Note: The statements, opinions and data contained in all publications are solely those of the individual author(s) and contributor(s) and not of MDPI and/or the editor(s). MDPI and/or the editor(s) disclaim responsibility for any injury to people or property resulting from any ideas, methods, instructions or products referred to in the content.